

Final Project Report

Group 24

Cristian Iaccovella

Mattia Li Vigni

Sara Moreira

Orbital Robotics and Distributed Space Systems
Politecnico di Torino

Contents

1	Introduction	4
1.1	Assumption	4
2	Orbital transfer to the debris position	6
2.1	Hohmann transfer analytical formulation	6
2.2	Hohmann transfer numerical integration	7
3	Relative dynamics final approach	13
3.1	Analytical solution of the Hill-Clohessy-Wiltshire equations	13
3.2	Numerical integration of the Hill-Clohessy-Wiltshire equations	15
4	Perturbations	18
4.1	Numerical propagation in equatorial CCS	19
4.2	Numerical propagation in the target Hill CCS	20
5	Robotic manipulator	23
5.1	Robotic Manipulator Design	23
5.2	Degrees of Freedom DOFs	24
5.3	Mathematical formulation	25
5.3.1	Kinematics	25
5.3.2	Differential Kinematics	26
5.3.3	Dynamics	28
5.4	Numerical Implementation	28
6	Impulse optimisation problem for the perturbed rendezvous	33
6.1	Preliminary considerations, fixed ToF	33
6.2	First version of the solution, fixed ToF	34
6.3	Second version of the solution, fixed ToF	35
6.4	Third version of the solution, variable ToF	36
7	Space debris retrieval and de-orbiting technologies	37
7.1	Deorbiting technologies trade-off	37
7.1.1	Thrusters	38

7.1.2	Solar sail	38
7.1.3	ElectroDynamic Tether	39
7.2	Results of the trade-off	40
7.3	ElectroDynamic Tether for debris removal in the considered case study	41
8	Conclusion	42
	References	43

Acronyms

ADR Active Debris Removal.

CCS Cartesian Coordinate System.

CoM Centre of Mass.

DCM Direction Cosine Matrix.

DOF Degree Of Freedom.

EDT ElectroDynamic Tether.

HCW Hill-Clohessy-Wiltshire.

HTM Homogeneous Transformation Matrix.

KR2BP Kepler Restricted 2-Body Problem.

ODE Ordinary Differential Equation.

S/C Spacecraft.

ToF Time of Flight.

TRL Technology Readiness Level.

1 Introduction

The objective of this work is to analyse the approach of a spacecraft (chaser) to a space debris (target), considering the orbital transfer, the proximity flight manoeuvre and a simplified capture scenario.

This report is organised as follows: in section 2, the transfer orbit between the chaser's and target's orbits is computed analytically and numerically. The numerical results are compared with the analytical ones to assess the accuracy of the numerical integration. The evolution of the constant of motion is evaluated both in the elliptical orbit and in the entire Hohmann transfer. Successively, in section 3, the relative dynamics and proximity flight are studied using the Hill-Chloessy-Whiltshire (HCW) equations. The results of the impulsive manoeuvre is computed both with analytical formulation and numerical integration, computing the minimum ΔV required for the manoeuvre and the associated time of flight (ToF). The effect of the perturbations due to atmospheric drag on the transfer orbit are considered in section 4. In section 5, a mathematical formulation for describing a 5 revolute degree of freedom (DOF) robotic manipulator is presented, along with a schematic of the manipulator design. The propagation of the contact force at the moment of the capture of the debris is computed. In section 6 some possible ways to design a successful rendezvous with the same perturbation of section 4 are presented. Space debris retrieval and deorbiting technologies are briefly presented in section 7, with a specific focus on deorbiting devices since, in the considered case study, the capture is performed with the robotic manipulator. Finally, section 8 concludes and sums up the study.

1.1 Assumption

This study is carried out under the following assumptions:

1. The spacecraft S/C (chaser) moves on an initial circular and equatorial orbit, with altitude $h_1 = 600 \text{ km}$ and radius R_1 .
2. The space debris D (target) is located on a second circular and equatorial orbit, with altitude of $h_2 = 350 \text{ km}$ and radius R_2 .
3. The initial phasing angle between the two orbiting objects is $\phi_0 = 10^\circ$.

Table 1 shows the set of data and assumptions used in the following computations. The orbital velocities are computed according to the formula derived from the equation of motion in the *Kepler Restricted 2-Body Problem* (KR2BP) for a circular orbit:

$$v = \sqrt{\frac{\mu}{R}} \quad (1)$$

where μ is the gravitational parameter of the primary (Earth) and R is the radius from the centre of Earth to the centre of mass of the object in orbit. The radii of the spacecraft and the debris are computed by adding to the (mean) Earth radius the altitude of the two objects.

Table 1: Initial data

Physical quantity	Symbol	Value	Unit of measure
Earth's gravitational parameter	μ	$3.9860 \cdot 10^5$	km^3/s^2
Earth's radius	R_{\oplus}	6378.1370	km
Radius of spacecraft's orbit	r_1	6978.1370	km
Radius of debris's orbit	r_2	6728.1370	km
Spacecraft's orbital velocity	v_1	7.5579	km/s
Debris' orbital velocity	v_2	7.6970	km/s
Drag coefficient	C_D	2.2	—
Chaser's cross-sectional area	A	2	m^2
Chaser's mass	m	325	kg

2 Orbital transfer to the debris position

The Hohmann transfer [1] is the most energy-efficient two-impulse manoeuvre for transferring between two coplanar circular orbits sharing a common focus. Therefore, the Hohmann transfer formulation is used to compute the minimum change of velocity Δv required to perform a two-impulse transfer from the satellite's initial position to the debris state.

2.1 Hohmann transfer analytical formulation

The required impulses are computed analytically according to the following formulas [2, 3]:

$$\Delta v_1 = \sqrt{\frac{\mu}{r_1}} \left(\sqrt{\frac{2r_2}{r_1 + r_2}} - 1 \right) = -0.0692 \text{ km/s} \quad (2)$$

$$\Delta v_2 = \sqrt{\frac{\mu}{r_2}} \left(1 - \sqrt{\frac{2r_1}{r_1 + r_2}} \right) = 0.0705 \text{ km/s} \quad (3)$$

The time of flight of the manoeuvre is:

$$ToF = \pi \sqrt{\frac{(r_1 + r_2)^3}{8\mu}} = 2823.0 \text{ s} = 47.05 \text{ min} \quad (4)$$

To conduct a correct approach between the chaser and the target, the angular displacement between the two must be taken into account. The ideal angular displacement between the chaser and the target is the one such that, while the chaser completes the transfer orbit, the debris sweeps out an angle which is exactly the initial phase of the chaser plus π . This angle is described by the following formula:

$$\phi_{phasing} = \sqrt{\frac{\mu}{r_1^3}} \cdot \pi \sqrt{\frac{(r_1 + r_2)^3}{8\mu}} - \pi = 0.0880 \text{ rad} = 5.0420^\circ \quad (5)$$

Considering the initial angle $\phi_0 = 10^\circ$ between the chaser and the target, the spacecraft has to wait before starting the Hohmann transfer, to arrive in the target orbit at the same position as the space debris. The waiting time is:

$$t_{wait} = \frac{\phi_0 - \phi_{phasing}}{n_2 - n_1} = 1421.1 \text{ s} = 23.68 \text{ min} \quad (6)$$

where the two n are the mean motions of the two bodies, computed as $n = \sqrt{\frac{\mu}{r^3}}$.

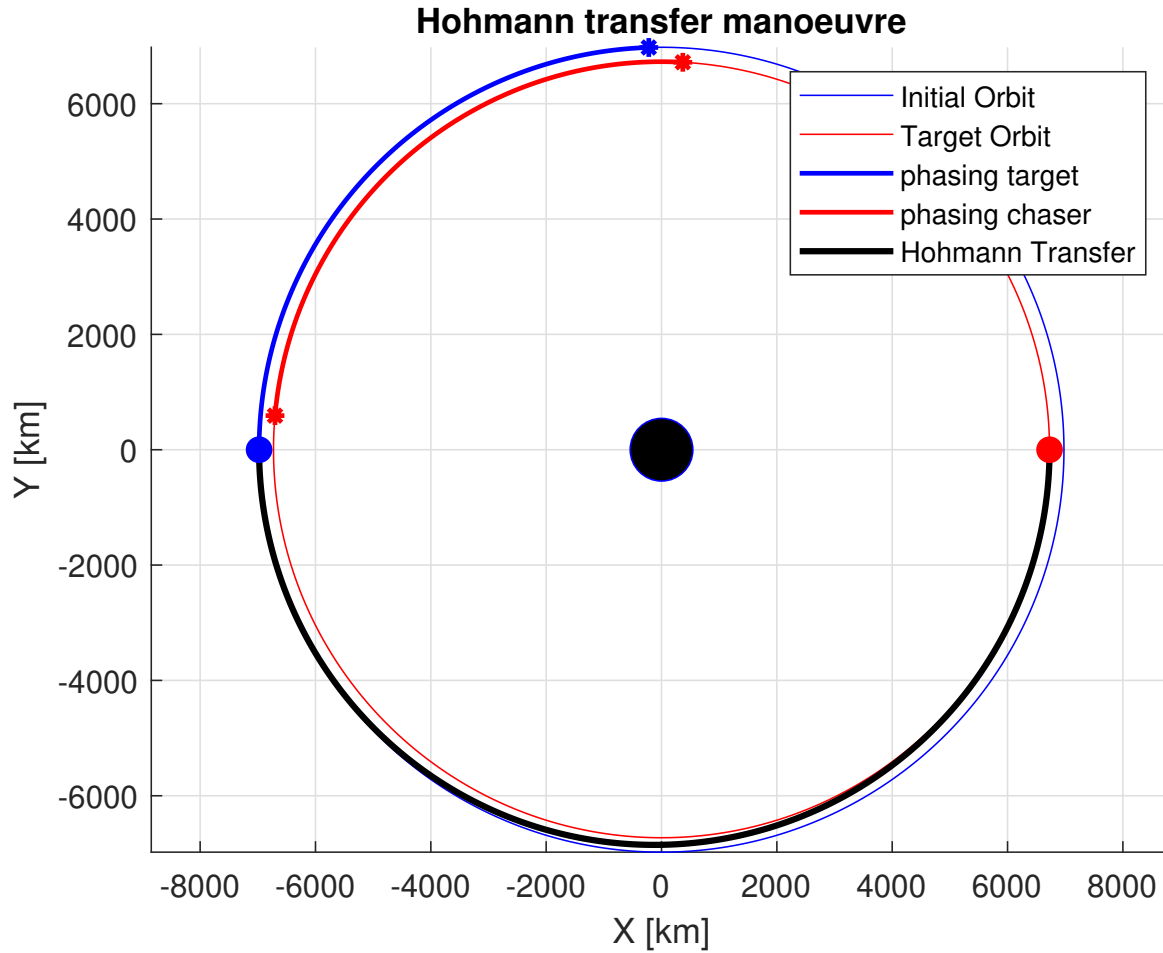


Figure 1: The plot shows the Hohmann transfer starting from the initial orbit and reaching the final orbit after sweeping out an angle equal to π . The orbit covered by the chaser and the target during the waiting time is highlighted with a thicker line.

Figure 1 plots the Hohmann transfer, showing both the initial and final orbit, and highlighting the portion of orbit travelled by the chaser and the target during the phasing time t_{wait} . Please note that, conventionally, a starting time is decided such that the Hohmann transfer starts when the chaser's true anomaly is $f_{S/C} = \pi$

2.2 Hohmann transfer numerical integration

The Hohmann transfer is also computed numerically using the ΔV values computed in the previous subsection 2.1. To do that, the differential equation of the Kepler restricted 2-body problem is solved numerically:

$$\ddot{\underline{r}} = -\mu \frac{\underline{r}}{r^3} \quad (7)$$

Firstly, a change of Cartesian coordinate systems is needed [4]. Starting from the orbital element, the

position and velocity vector are derived in the Hill reference frame \mathbb{H} . The analytical Δv_1 computed in Equation 2 is added to the absolute velocity vector $\dot{\underline{r}}^H$. Then the position vector \underline{r}^H and the velocity vector $\dot{\underline{r}}^H$ are rotated in the perifocal vector base (\underline{r}^P and $\dot{\underline{r}}^P$) and successively in the equatorial vector base (\underline{r}^E and $\dot{\underline{r}}^E$). Please note that the change of CCS from perifocal to equatorial is not needed in this specific case study since inclination i , RAAN (Right Ascension of the Ascending Node) Ω and argument of periapsis ω are all null.

\underline{r}^E and $\dot{\underline{r}}^E$ are the initial condition for the numerical computation, which is performed through a numerical integrator: `MatLab's ode113`; please note that the standard settings are changed, decreasing the tolerance, in order to increase the accuracy of the numerical integration. The standard substitution for a system of ordinary differential equations (ODE) is used, with $z(1) = x$, $z(2) = y$ and $z(3) = z$; please note that the z on the left handside of the previous equivalences is the function used of the system of ODE while the one on the right handside is the coordinate in the equatorial reference frame. The system of equations is the following:

$$\begin{aligned}\dot{z}(1) &= z(4) \\ \dot{z}(2) &= z(5) \\ \dot{z}(3) &= z(6) \\ \dot{z}(4) &= -\mu \frac{z(1)}{\sqrt{(z(1)^2 + z(2)^2 + z(3)^2)^3}} \\ \dot{z}(5) &= -\mu \frac{z(2)}{\sqrt{(z(1)^2 + z(2)^2 + z(3)^2)^3}} \\ \dot{z}(6) &= -\mu \frac{z(3)}{\sqrt{(z(1)^2 + z(2)^2 + z(3)^2)^3}}\end{aligned}$$

An additional equation is added to compute the numerical propagation of the true anomaly f [4]:

$$\dot{z}(7) = \dot{f} = \frac{h}{r^2} = \frac{h}{\sqrt{z(1)^2 + z(2)^2 + z(3)^2}}$$

where h is the norm of the angular momentum and r is the norm of the radius vector.

The numerical propagation is performed for a timespan equal to the time of flight computed in Equation 4 and with \underline{r}^E and $\dot{\underline{r}}^E$ as initial conditions for the position and velocity vector and $f = \pi$ as initial condition for the true anomaly.

As a result of the numerical integration, a set of positions (\underline{r}_{num}) and velocities ($\dot{\underline{r}}_{num}$), and true anomalies is derived. They can be compared with the analytical results derived in subsection 2.1. It can be done by substituting the values of the true anomalies computed into the analytical parameterisation of the elliptical transfer. Figure 2a plots the two orbits, graphically highlighting the precise approximation of the numerical solution with respect to the analytical one.

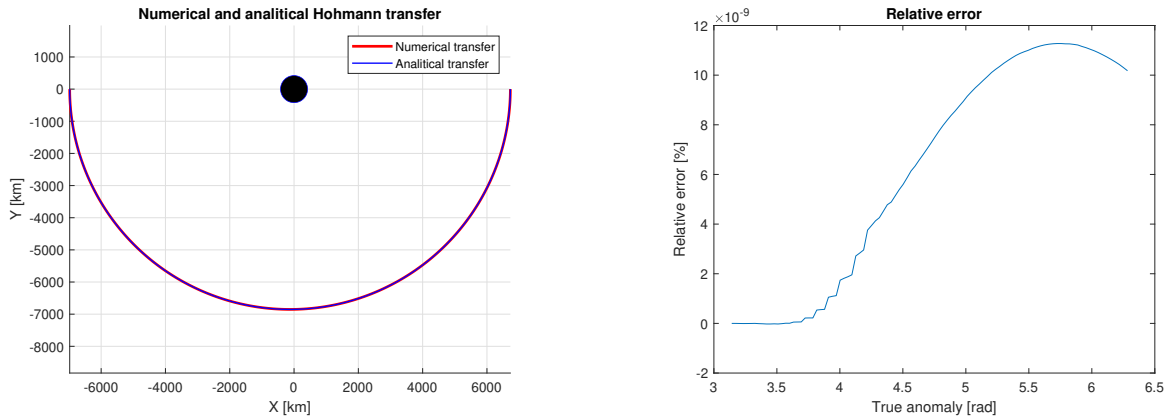
A more accurate comparison can be performed by evaluating the error between the analytical and numerical radii. The radius of the elliptical orbit can be parametrised with the following equation:

$$r_{analytic} = \frac{a(1 - e^2)}{1 + e \cos(f)} \quad (8)$$

where the semi-major axis is $a = \frac{R1+R2}{2} = 6853.1370 \text{ km}$, the eccentricity is $e = \frac{R1-R2}{R1+R2} = 0.0182$, and f is the true anomaly (in rad).

The relative error between the radius of the elliptical orbit calculated with numerical integration and the analytical formulation is the following:

$$e_{rel} = \frac{r_{analytic} - r_{num}}{r_{analytic}} \quad (9)$$



(a) Graphical comparison between the numerical and analytical Hohmann transfer. The two elliptical orbits almost overlap in the entire trajectory, highlighting the high fidelity of the numerical integration.

(b) Relative error e_{rel} between the analytic and numerical radius of the Hohmann elliptical orbit. The few discrepancies between the analytical and numerical results are supposed to be due to numerical errors.

Figure 2: Comparison between the analytic and numeric Hohmann transfer.

The value of e_{rel} is reported as a function of the true anomaly f in Figure 2b, highlighting the very low difference between the analytical and numerical results. The discrepancy is supposed to be due to numerical errors.

To further assess the accuracy of the numerical integration, the evolution in time of the constants of motion (angular momentum \underline{h} , eccentricity vector \underline{e} , and total orbital energy ϵ) is analysed. They should be constant in an ideal problem without perturbation, like the one studied. Figure 3 plots the time evolution of the constant of motion: angular momentum norm, eccentricity vector norm, and total orbital energy. It can be observed that they are not perfectly constant since numerical errors may occur; however, their displacement from the ideal value of the analytical solution is low, with the maximum relative error between the ideal and numerical solution being approximately $1 \cdot 10^{-5}$ % for the eccentricity and $1 \cdot 10^{-7}$ % for the angular momentum and orbital energy.

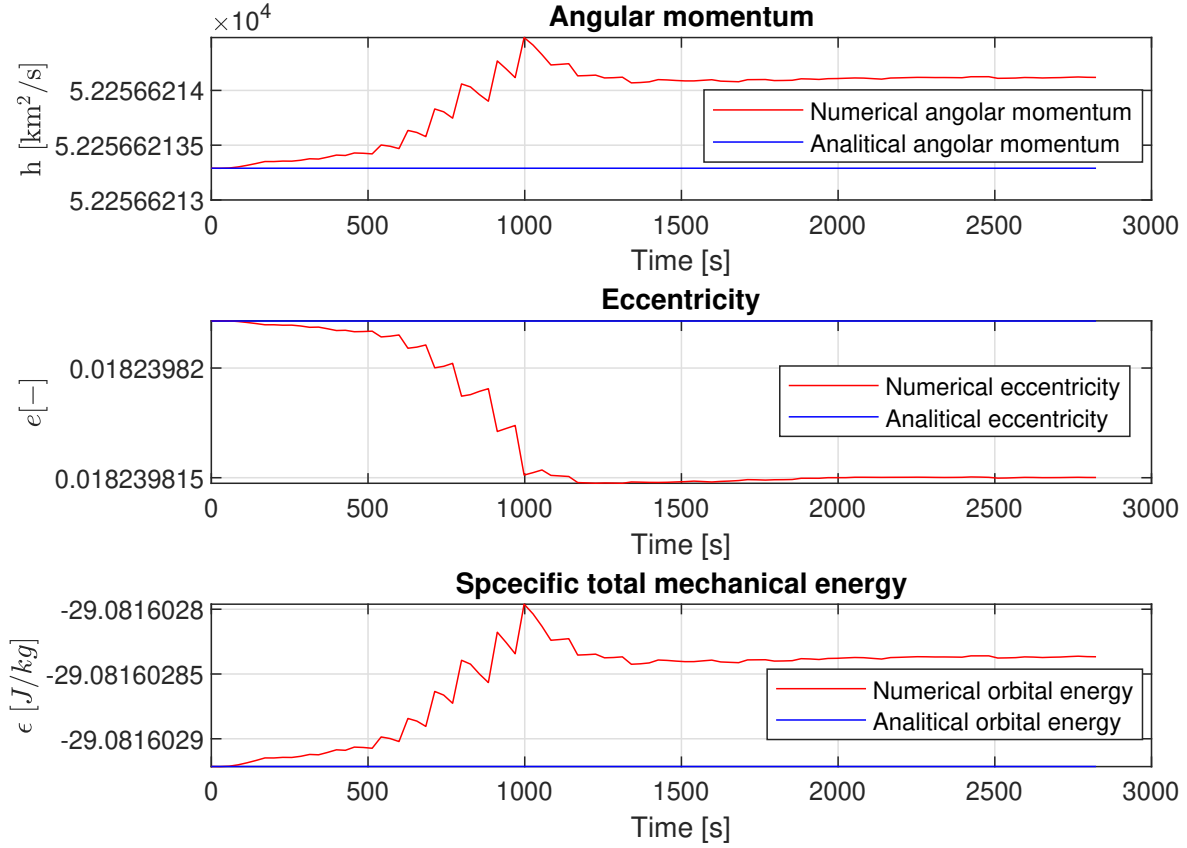


Figure 3: Temporal evolution of the constants of motion: angular momentum norm, eccentricity vector norm, and total orbital energy. All the constants have very slight variations in time and have values close to the one expected from the analytical results.

Successively, the entire transfer, from the starting position to the final position after one orbital period, is computed numerically. To do so, a step-by-step integration is performed, adding the impulsive velocity to the velocity vector at the end of the previous integration. The first integration starts with the initial condition (position and orbital velocity at the starting point). The numerical propagation is performed for a timestep of $t = t_{wait}$ (see Equation 6). The integration is stopped, and the analytical Δv_1 (Equation 2) is added to the velocity vector at the end of the integration. The Δv has to be added to the component tangential to the orbit. To do so, it is necessary to add to the velocity vector another vector parallel to the previous one and with a norm equal to Δv_1 . It is possible to consider that two parallel vectors are proportional, so one can easily sum the two.

After changing the initial condition, the second integration is performed, considering the impulse. The timespan ranges from $t = t_{wait}$ to $t = t_{wait} + ToF$ (see Equation 4). At the end of the numerical propagation, the second impulse is considered to change again the initial condition for the last integration, which is performed until the end of the orbital period. The graphical results are shown in Figure 4. Please note that in this second numerical integration, the starting point (blue dot) is starting from a true anomaly of $f = 0^\circ$, which is different from the previous one shown in subsection 2.1.

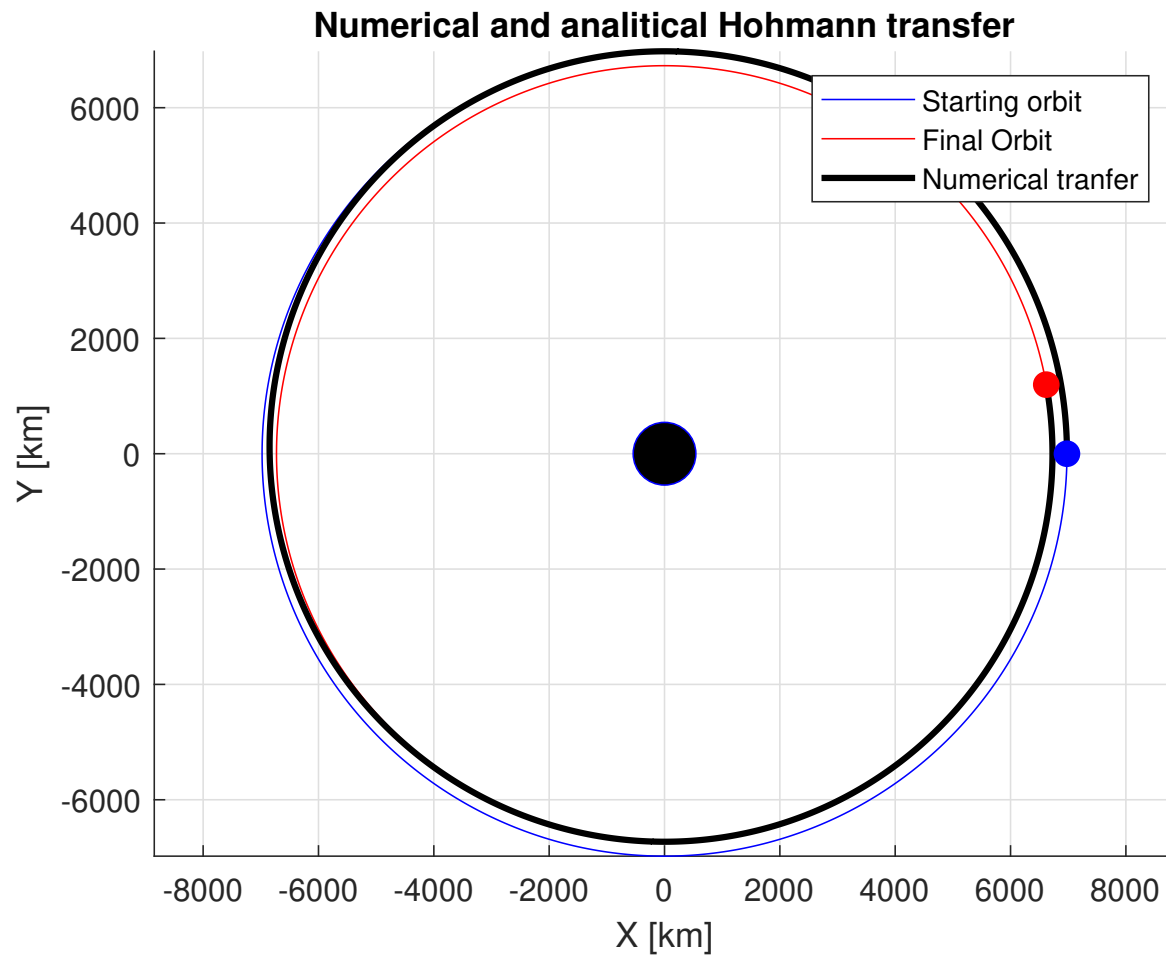


Figure 4: Numerical integration of the full Hohmann transfer taking into account also the starting and the final orbit. It can be observed that the results overlap with the analytical starting and final orbits.

The constants of motion are also computed for the full transfer. It can be observed from Figure 5 how they change during the entire manoeuvre.

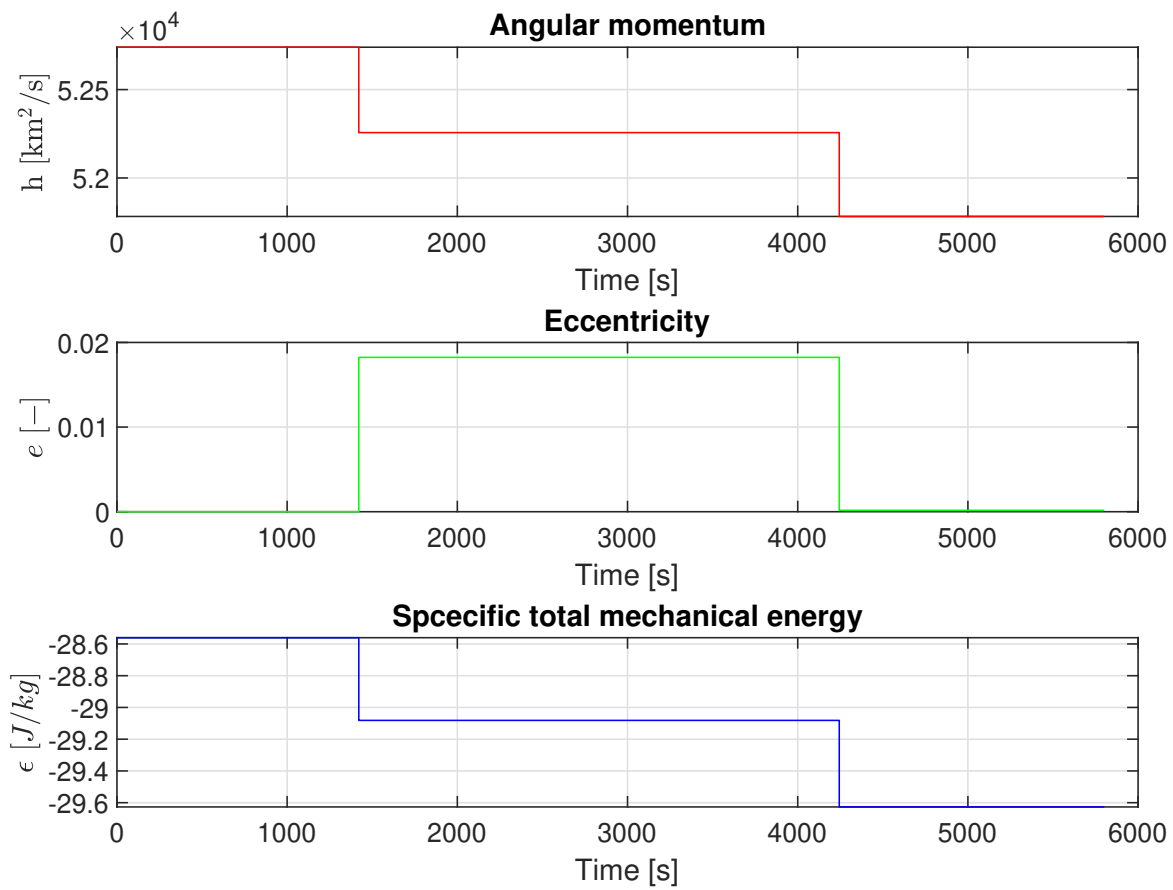


Figure 5: Temporal evolution of the constant of motion during the full Hohmann transfer. It can be observed how they are constant during the single orbit and change after the impulsive manoeuvre.

3 Relative dynamics final approach

In a more realistic scenario, the spacecraft does not perform a perfect rendezvous; therefore, the relative distance and velocity at the end of the manoeuvre are not zero. To study the relative dynamics, the adimensional Hill-Clohessy-Wiltshire (HCW) [5] equations are used:

$$\ddot{\xi} - 3\xi - 2\dot{\eta} = 0 \quad (10)$$

$$\ddot{\eta} + 2\dot{\xi} = 0 \quad (11)$$

$$\ddot{\zeta} + \zeta = 0 \quad (12)$$

Where $\xi = \frac{x}{L}$, $\eta = \frac{y}{L}$, and $\zeta = \frac{z}{L}$ are the adimensional position variables (L is a constant characteristic length, in this case the radius of the target's orbit). Time is normalised using the inverse of the target's mean motion, therefore, velocity is normalised by dividing by both the radius and the mean motion of the target. The HCW equations hold for circular orbits and a relative distance between the chaser and the target much smaller than the radius of the target orbit. Both of these assumptions are verified in the considered scenario.

3.1 Analytical solution of the Hill-Clohessy-Wiltshire equations

It can be observed that Equation 10 and Equation 11 are decoupled from Equation 12. Therefore, they can be solved independently. The *state transition matrix* ϕ needed to solve the problem can be derived both for the third equation (12) and the first and the second (10 and 11). Since in this Kepler Restricted 2-Body Problem the motion is in the $\xi\eta$ plane, the ζ component is always zero; therefore, only the ϕ_P to solve Equation 10 and 11 is here reported [4]:

$$\Phi_P(f, f_0) = \begin{bmatrix} 4 - 3\cos(f - f_0) & \sin(f - f_0) & 0 & 2 - 2\cos(f - f_0) \\ 3\sin(f - f_0) & \cos(f - f_0) & 0 & 2\sin(f - f_0) \\ -6(f - f_0) + 6\sin(f - f_0) & -2 + 2\cos(f - f_0) & 1 & -3(f - f_0) + 4\sin(f - f_0) \\ -6 + 6\cos(f - f_0) & -2\sin(f - f_0) & 0 & -3 + 4\cos(f - f_0) \end{bmatrix}$$

Where f is the normalised time and f_0 is the initial epoch.

The analytical solutions of the HCW are then computed as follows:

$$\begin{bmatrix} \xi(f) \\ v_\xi(f) \\ \eta(f) \\ v_\eta(f) \end{bmatrix} = \Phi_P(f, f_0) \begin{bmatrix} \xi(f_0) \\ v_\xi(f_0) \\ \eta(f_0) \\ v_\eta(f_0) \end{bmatrix}$$

By letting $f_0 = 0$ and imposing the relative position equal to zero at the end of the rendezvous in the analytical solutions of the HCW, the relative velocity vector components after the first impulse can be calculated as follows:

$$v_{\xi_0}^+ = \frac{-2\eta_0 + (2\eta_0 - 3\bar{f}\xi_0) \cos(\bar{f}) + 4\xi_0 \sin(\bar{f})}{3\bar{f} \sin(\bar{f}) + 8 \cos(\bar{f}) - 8} \quad (13)$$

$$v_{\eta_0}^+ = \frac{14\xi_0 - 14\xi_0 \cos(\bar{f}) + (\eta_0 - 6\bar{f}\xi_0) \sin(\bar{f})}{3\bar{f} \sin(\bar{f}) + 8 \cos(\bar{f}) - 8} \quad (14)$$

$$v_{\zeta_0}^+ = -\frac{\cos(\bar{f})}{\sin(\bar{f})} \zeta_0 \quad (15)$$

Where \bar{f} is a priori chosen maneuver duration time (expressed in normalised units) and $v_{\xi_0}^+$, $v_{\eta_0}^+$ and $v_{\zeta_0}^+$ are the velocity components after the first impulse. ξ_0 , η_0 , and ζ_0 are the adimensional initial positions in the Hill reference frame.

The first Δv is the difference between the velocity after and before this impulse:

$$\Delta v_0 = v_0^+ - v_0^- \quad (16)$$

Note that the initial conditions in terms of velocity and position in the in-plane direction are computed as a random error.

In order to choose a certain two-impulse rendezvous, first the velocities after the first impulse are computed for different values of maneuver duration \bar{f} using Equation 13, 14 and 15; with these quantities Δv_0 is computed according to Equation 16, using the randomly generated velocity as v_0^- .

The second impulse $\Delta v_{\bar{f}}$ is the one such that the relative velocity at normalised time \bar{f} is nullified:

$$\Delta v_{\bar{f}} = -v(\bar{f}) \quad (17)$$

$v(\bar{f})$ is obtained by calculating the analytical solution using the velocity vector after the first impulse in the initial condition.

The total ΔV for the two impulses is given by:

$$\Delta V = \|\Delta \mathbf{v}_f\| + \|\Delta \mathbf{v}_0\|$$

We used norm-2, assuming that a single directional thruster is used (norm-1 is used for a cluster of multiple body-fixed thrusters).

The result of this analysis is plotted in Figure 6. This study was used to choose a certain two-impulse manoeuvre, we decided to use the time of flight with the minimum associated ΔV .

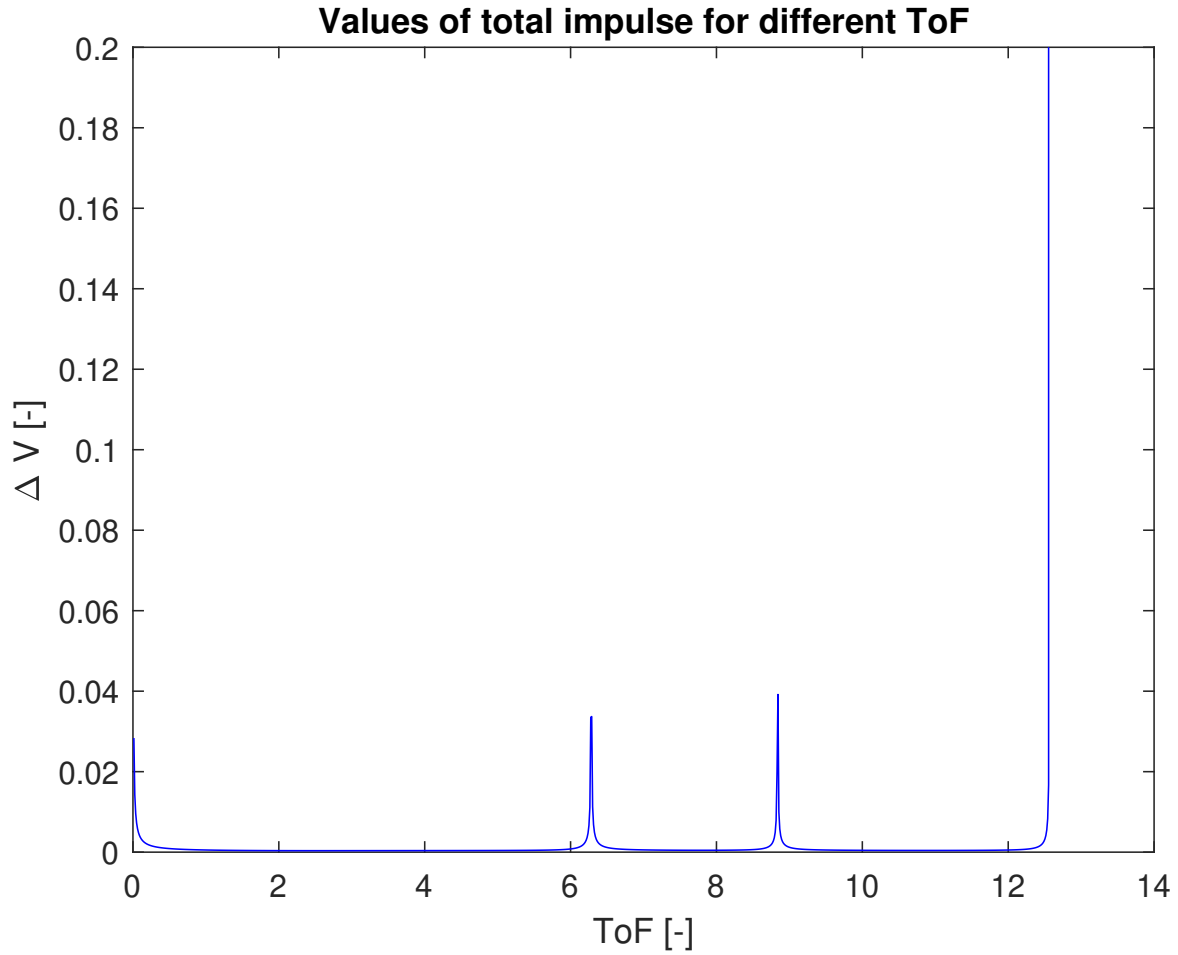


Figure 6: Total impulse necessary for the rendezvous against the time of flight of the manoeuvre.

The minimum ΔV required for the manoeuvre is:

$$\Delta V_{min} = 2.4792 \text{ km/s} \quad (18)$$

The time of flight of the minimum ΔV manoeuvre is:

$$ToF_{min\Delta V} = 2199.1140s = 36.65 \text{ min} \quad (19)$$

3.2 Numerical integration of the Hill-Clohessy-Wiltshire equations

The system of ODE for the numerical integration of the HCW equations is as follows:

$$\begin{aligned}
\dot{z}(1) &= z(2) \\
\dot{z}(2) &= 3z(1) + 2z(4) \\
\dot{z}(3) &= z(4) \\
\dot{z}(4) &= -2z(2) \\
\dot{z}(5) &= z(6) \\
\dot{z}(6) &= -z(5)
\end{aligned}$$

where $z(1) = \xi$, $z(3) = \eta$, $z(5) = \zeta$.

The initial condition for the numerical integration of the HCW equations is derived by summing the previous random initial condition with Δv_0 derived in subsection 3.1, which is the first impulse of the manoeuvre associated with the chosen time of flight. The following graphs show the absolute difference between the solution obtained via numerical propagation and the analytical one.

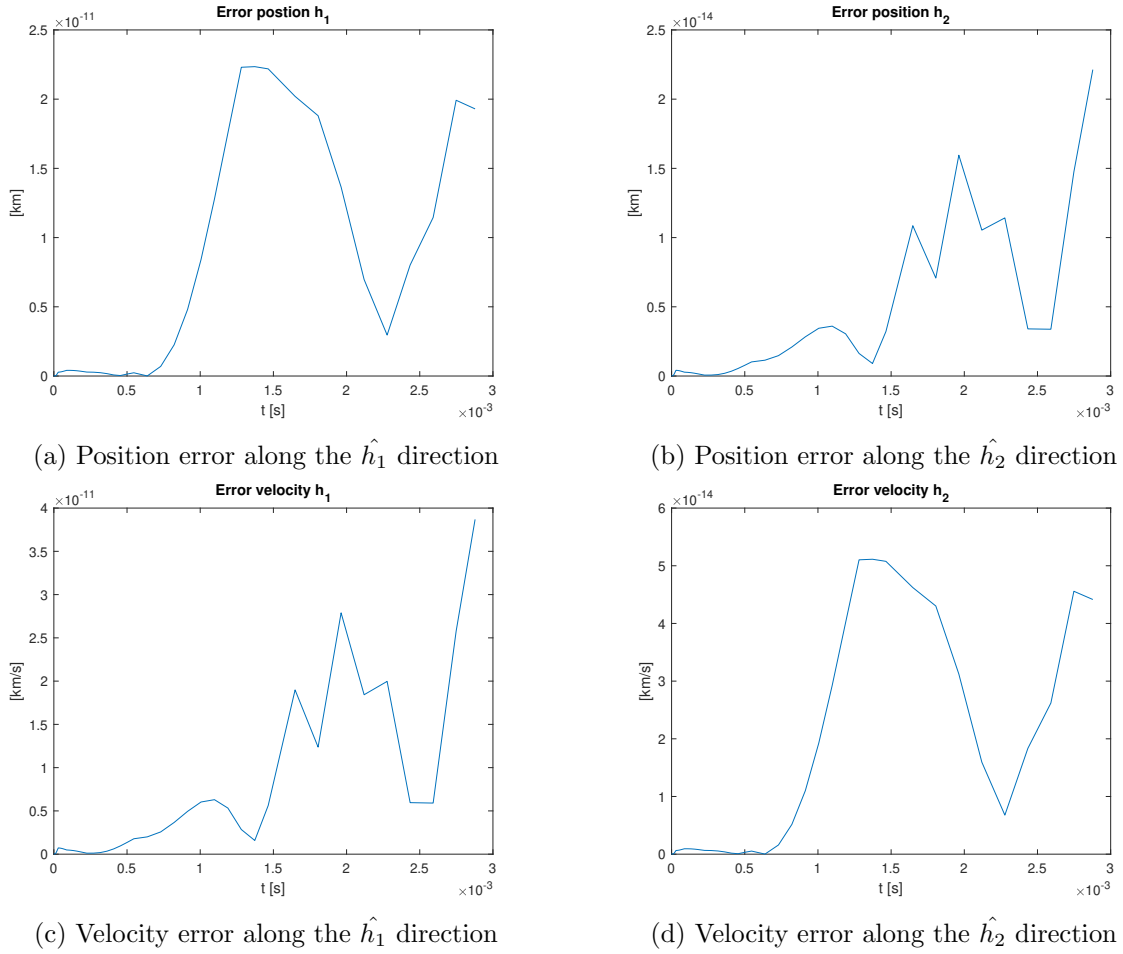
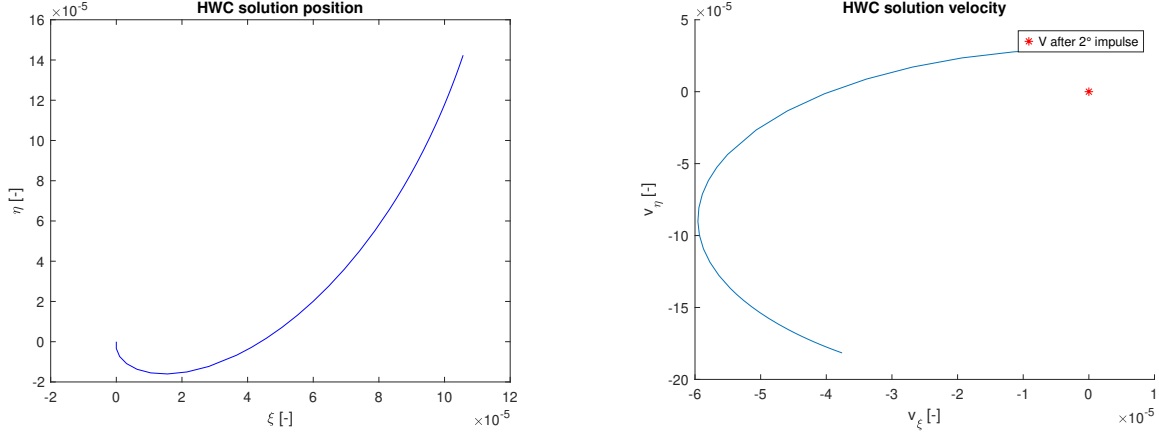


Figure 7: Comparison between the analytical and numerical solution of the Hill-Clohessey-Wiltshire equations. The errors in position and velocity in both axes in the Hill reference frame are low and are supposed to be only due to numerical errors.

The evolution of the position (8a) and the velocity (8b) of the spacecraft in the Hill reference frame (numerical solution) are reported in the two subfigures in Figure 8. At the end of the rendezvous, the final position is at the origin of the Hill CCS. In the other graph, it is shown how the relative velocity becomes zero only after the second impulse.



(a) Trajectory evolution in the Hill reference frame

(b) Velocity evolution in the Hill reference frame

Figure 8: Evolution of the trajectory and the velocity of the spacecraft in the Hill reference frame

4 Perturbations

A more realistic model taking into account the perturbations is considered:

$$\ddot{\underline{r}} + \mu \frac{\underline{r}}{r^3} = \underline{d} \quad (20)$$

Some of the most relevant perturbations are:

1. Earth's oblateness (J2)
2. Atmospheric drag
3. Solar radiation pressure
4. Third-body effects (Moon, Sun)

The first one is not present since the orbit is equatorial, furthermore, solar radiation pressure and third-body effects are, in this scenario, assumed negligible compared to atmospheric drag in Low Earth Orbit (LEO). Artificial satellites in LEO encounter a residual atmosphere, with a density that is so low that the air does not exhibit a continuous fluid behaviour: the flow regime is called free molecular flow. A first-order approximation of the phenomenon for the aerodynamic drag acceleration is:

$$\underline{d}_D = -\frac{1}{2} \frac{C_D A}{m} \rho V \underline{V} \quad (21)$$

Where ρ is the density of the residual atmosphere, V is the relative velocity of the satellite with respect to the atmosphere, C_D is the drag coefficient, A is the cross-sectional area of the satellite, and m is its mass. In this equation both the lift and the corotation are neglected (hence the absolute velocity of the satellite is the same as its relative velocity with the atmosphere).

$$\ddot{x} = -\mu \frac{x}{r^3} - \frac{1}{2} \frac{C_D A}{m} \rho v \dot{x} \quad (22)$$

$$\ddot{y} = -\mu \frac{y}{r^3} - \frac{1}{2} \frac{C_D A}{m} \rho v \dot{y} \quad (23)$$

$$\ddot{z} = -\mu \frac{z}{r^3} - \frac{1}{2} \frac{C_D A}{m} \rho v \dot{z} \quad (24)$$

Where $v = \sqrt{\dot{x}^2 + \dot{y}^2 + \dot{z}^2}$.

The value of the density depends on the altitude and changes depending on whether it is day or night, the season, the sun cycle, and space weather events. In this analysis, the density in the specific table in "U.S. Standard Atmosphere, 1976" [6] is used as a reference; this value provides a reasonable estimation for a general design of a mission. Therefore, at an altitude of 350 km (assumed constant since it is a final approach in close proximity to the target), the density is $\rho = 7.014 \cdot 10^{-12}$ kg/m³.

In this section, the effect of the atmospheric drag on the rendezvous is evaluated. The same analytical impulse found in section 3 can be applied to find the final offset in terms of position and velocity with respect to the desired state. The perturbation is assumed to affect only the chaser, which has a cross-sectional area of 2 m² and a mass of 325 kg. For the drag coefficient the standard value of 2.2 is considered.

4.1 Numerical propagation in equatorial CCS

Firstly, the Equation 22, 23, and 24 are propagated numerically in the inertial reference frame. Since the rendezvous is calculated only by solving the HCW equations, the unperturbed rendezvous is first verified in the equatorial Cartesian Coordinate System (CCS). The initial condition for the chaser is its position and velocity after the first impulse. To transform its velocity from the target Hill reference frame to the equatorial frame, the chaser's relative velocity, the target's velocity in equatorial CCS and the contribution given by the target's angular velocity cross-multiplied by the chaser's relative position are summed.

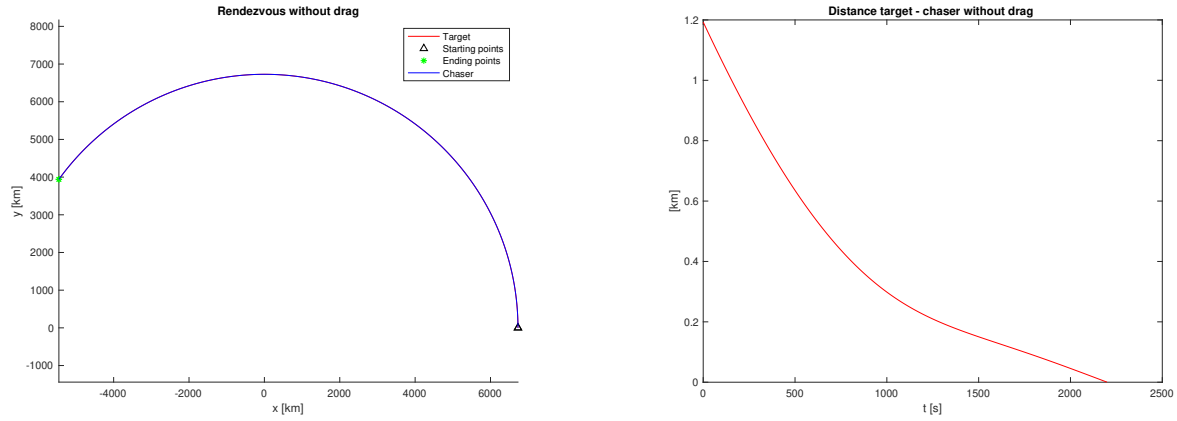


Figure 9: Unperturbed rendezvous in the equatorial CCS. The first graph aims to give a general idea of the rendezvous in the equatorial CCS, the second graph is used to show the relative distance which could not be seen due to the scale of the figure.

The numerical integration, in the selected case, shows a final position offset of 0.3581 m, which is reasonable since, as we have already discussed, the HCW equations are an approximation.

Successively, the perturbed equations (see Equation 22, 23, 24) in the equatorial CCS are numerically propagated using a standard substitution to solve the system of ODEs.

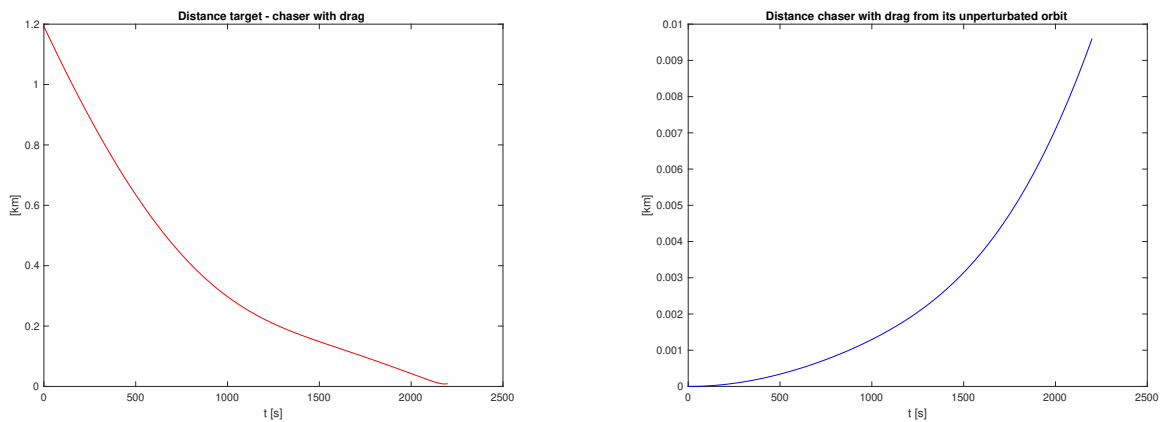


Figure 10: Perturbed rendezvous in the equatorial CCS and drag effect on the chaser position with respect to its unperturbed orbit

The numerical integration for the perturbed rendezvous, in the selected case, shows a final position offset of 9.2454 m. The final offset is computed in terms of velocity (after the second impulse) with respect to the desired state only in the target Hill CCS.

4.2 Numerical propagation in the target Hill CCS

In this section, the analysis in the target's Hill CCS is presented. Similarly to what was discussed in section 3, the target's orbit is circular, and the relative distance from the chaser is much smaller than the radius of the target's orbit. The equations describing the relative dynamics in the perturbed case are derived in this section.

$$\begin{aligned}\ddot{\underline{r}}_t &= -\mu \frac{\underline{r}_t}{r_t^3} \\ \underline{\rho} &= \underline{r}_c - \underline{r}_t \\ \ddot{\underline{r}}_c &= -\mu \frac{\underline{r}_c}{r_c^3} - \underline{d}_D = -\mu \frac{\underline{r}_t + \underline{\rho}}{\|\underline{r}_t + \underline{\rho}\|^3} - \underline{d}_D\end{aligned}$$

Where the dot symbol indicates the derivative in the equatorial reference frame (\mathbb{N}). ρ can be derived in \mathbb{N} as follows:

$$\ddot{\underline{\rho}} = \ddot{\underline{r}}_c - \ddot{\underline{r}}_t = -\mu \frac{\underline{r}_c}{r_c^3} - \underline{d}_D + \mu \frac{\underline{r}_t}{r_t^3}$$

The empty dot symbolises the time derivative in the target Hill reference frame (\mathbb{H}).

$$\begin{aligned}\dot{\underline{\rho}} &= \dot{\underline{\rho}} + \underline{\omega}_{\mathbb{H}\mathbb{N}} \times \underline{\rho} \\ \ddot{\underline{\rho}} &= \ddot{\underline{\rho}} + 2\underline{\omega}_{\mathbb{H}\mathbb{N}} \times \dot{\underline{\rho}} + \dot{\underline{\omega}}_{\mathbb{H}\mathbb{N}} \times \underline{\rho} + \underline{\omega}_{\mathbb{H}\mathbb{N}} \times \underline{\omega}_{\mathbb{H}\mathbb{N}} \times \underline{\rho} \\ \ddot{\underline{\rho}} &= -\mu \frac{\underline{r}_c}{r_c^3} - \underline{d}_D + \mu \frac{\underline{r}_t}{r_t^3} - 2\underline{\omega}_{\mathbb{H}\mathbb{N}} \times \dot{\underline{\rho}} - \dot{\underline{\omega}}_{\mathbb{H}\mathbb{N}} \times \underline{\rho} - \underline{\omega}_{\mathbb{H}\mathbb{N}} \times \underline{\omega}_{\mathbb{H}\mathbb{N}} \times \underline{\rho}\end{aligned}$$

Where $\underline{\omega}_{\mathbb{H}\mathbb{N}} = \dot{f}\hat{h}_3$ and $\dot{\underline{\omega}}_{\mathbb{H}\mathbb{N}} = \ddot{f}\hat{h}_3$.

In the target Hill frame with vector base $\hat{e}^{\mathbb{H}} = \begin{Bmatrix} \hat{h}_1 \\ \hat{h}_2 \\ \hat{h}_3 \end{Bmatrix}$, $\rho^{\mathbb{H}} = \begin{Bmatrix} \hat{x} \\ \hat{y} \\ \hat{z} \end{Bmatrix}$. The equations of motion describing the dynamics of the chaser in the target Hill CCS are as follows:

$$\begin{aligned}\ddot{x} - 2\dot{f}\dot{y} - \ddot{f}y - \dot{f}^2x &= -\mu \frac{x + r_t}{r_c^3} + \frac{\mu}{r_t^2} - d_{Dx} \\ \ddot{y} + 2\dot{f}\dot{x} + \ddot{f}x - \dot{f}^2y &= -\mu \frac{y}{r_c^3} - d_{Dy} \\ \ddot{z} &= -\mu \frac{z}{r_c^3} - d_{Dz}\end{aligned}$$

The drag acceleration is the same as indicated in section 4; it is projected along the 3 components of the target Hill CCS. The velocity considered is derived as follows:

$$\underline{V} = \underline{\dot{r}}_c = \underline{\dot{\rho}} + \underline{\dot{r}}_t = \underline{\dot{\rho}} + \underline{\omega_{\text{HIN}}} \times \underline{\rho} + \underline{\dot{r}}_t \quad (25)$$

Since the target's orbit is circular $\omega_{\text{HIN}} = \dot{f} = \sqrt{\frac{\mu}{r_t^3}} = \text{cost}$, $r_t = \text{cost}$, $r_c = \sqrt{(r_t + x)^2 + y^2 + z^2}$. The second hypothesis is that $\frac{\rho}{r_t} \ll 1$ therefore $r_c^{-3} \sim r_t^{-3}(1 - \frac{3x}{r_t})$.

The equations can be rewritten as follows:

$$\begin{aligned} \ddot{x} - 2\sqrt{\frac{\mu}{r_t^3}}\dot{y} - \frac{\mu}{r_t^3}x &= -\mu(x + r_t)r_t^{-3}(1 - \frac{3x}{r_t}) + \frac{\mu}{r_t^2} - d_{Dx} \\ \ddot{y} + 2\sqrt{\frac{\mu}{r_t^3}}\dot{x} - \frac{\mu}{r_t^3}y &= -\mu yr_t^{-3}(1 - \frac{3x}{r_t}) - d_{Dy} \\ \ddot{z} &= -\mu zr_t^{-3}(1 - \frac{3x}{r_t}) - d_{Dz} \end{aligned}$$

After some algebraic passages and by neglecting the second order infinitesimals (in this case, the factors multiplied by x^2, xy, xz), the equations are:

$$\begin{aligned} \ddot{x} - 2n\dot{y} - 3n^2x &= -d_{Dx} \\ \ddot{y} + 2n\dot{x} &= -d_{Dy} \\ \ddot{z} + n^2z &= -d_{Dz} \end{aligned}$$

Where $n = \sqrt{\frac{\mu}{r_t^3}}$ and the drag perturbation components are calculated by projecting the velocity written in equation 25 along the target Hill frame axes. In order to numerically integrate, a standard substitution is needed to have a system of 6 ODEs similarly as what was done for the HCW equations.

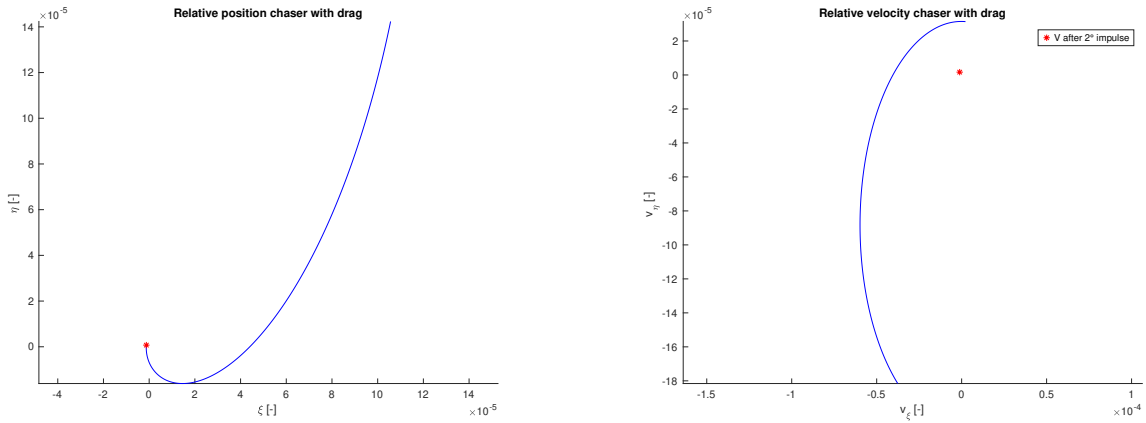


Figure 11: Rendezvous with drag perturbation on the chaser solved in the target Hill CCS

The numerical integration for the perturbed rendezvous in the target Hill CCS, in the considered case, yields a final position offset of 9.6018 m; the difference in value compared to the integration in the equatorial CCS can be attributed to the previously described assumptions. The final velocity offset after the second impulse is $13.6222 \frac{m}{s}$.

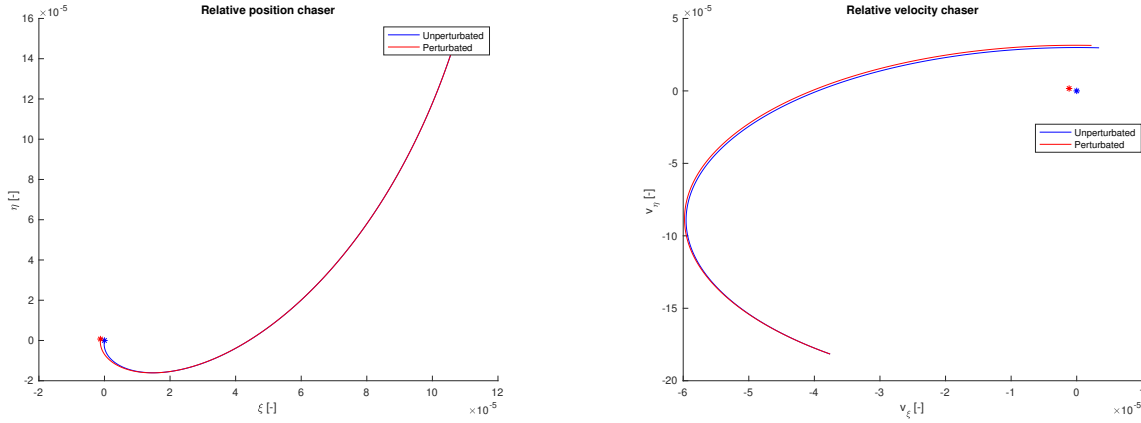


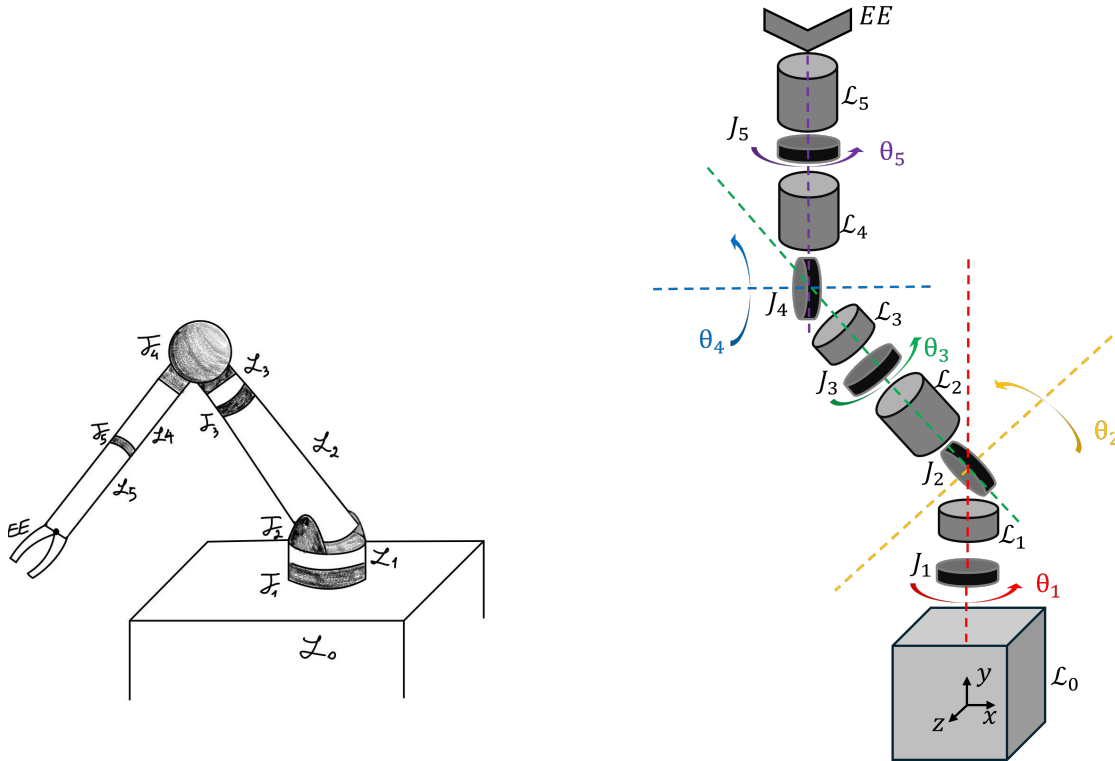
Figure 12: Comparison of position and velocity between perturbed and unperturbed rendezvous solved in the target Hill CCS. The stars symbolise the final states after the second impulse.

5 Robotic manipulator

In the considered case study, the spacecraft is equipped with a 5-revolute degree-of-freedom (DOF) robotic manipulator. Therefore, the overall multi-body system consists of a base, 5 joints \mathcal{J} and 5 links \mathcal{L} connecting the joints.

5.1 Robotic Manipulator Design

The choice of the geometry, mass properties and joint motors is one of the most complex parts in a space robotic manipulator design phase. It is possible to apply sophisticated methods, like solving an optimisation problem where the cost function represents the weight of the robotic arm [7]. However, for the sake of simplicity, a less complex approach is adopted here. Some famous robotic missions are considered to understand if a similar design can be used in the considered case study. The two main missions analysed are ETS-VII [8, 9] and Orbital Express [10]. However, the robotic arms used in these missions are too big and heavy for a spacecraft of the dimensions and mass ($m = 325$ kg) considered. Therefore, the inspiration is drawn from two lighter and smaller solutions: LWR III [11] and ROKVISS [12] from DLR (German Space Agency). The robotic manipulator proposed has similar mass and geometrical properties to LWR III.



(a) Sketch of the robotic arm. The joints \mathcal{J}_i are highlighted in grey, and the links \mathcal{L}_i and the end effector EE are in white.

(b) Schematic representation of the links (grey) and joints (black). The rotational axes of each joint are highlighted in different colours.

Figure 13: Sketch and schematic representation of the robotic arm; it consists of two successive spherical wrists attached to a free-moving base (the spacecraft).

A preliminary sketch of the robotic manipulator considered is reported in Figure 13a, while Figure 13b shows a schematic representation of the joints and links of the manipulator. For the sake of simplicity, the joints are considered massless and volumeless, while the links are approximated with a cylindrical shape. This robotic arm can be considered as composed of 2 successive spherical wrists with one rotational axis (the one of the joint \mathcal{J}_3). This solution allows for dexterous manipulation and a wide range of motion. Moreover, by using three consecutive joint axes intersecting at a single point (e.g. a spherical wrist), it is possible to have a solution in closed form in the Inverse Kinematics Problem.

The geometrical and mass properties of the link, such as mass, radii, length and the moment of inertia along the principal axes, are reported in Table 2. For the sake of simplicity, all the links are made of the same aluminium alloy 7075, which is commonly used for aerospace applications. Its density is $\rho_{Al} = 2.81 \text{ g/cm}^3$.

Table 2: Geometrical and mass properties of the link

Link Number	m [kg]	r [mm]	L [m]	I_1 [kg m ²]	$I_2 = I_3$ [kg m ²]
\mathcal{L}_1 & \mathcal{L}_3	0.7	40	0.05	$0.57 \cdot 10^{-3}$	$0.15 \cdot 10^{-3}$
\mathcal{L}_2 & \mathcal{L}_4 & \mathcal{L}_5	4.2	40	0.30	$3.39 \cdot 10^{-3}$	$31.80 \cdot 10^{-3}$

The overall mass of the robotic arm is about 14 kg while the overall length is about 1 m.

Please note that the robotic arm described in this section is designed for 3D motion and its Degrees of Freedom (DOFs) are studied in a 3D space in subsection 5.2. However, for the sake of simplicity, it is studied in a planar case (2D) in subsection 5.4. To do so, the angular displacement of the joints \mathcal{J}_1 , \mathcal{J}_3 and \mathcal{J}_5 are null ($\theta_1 = \theta_3 = \theta_5 = 0 \text{ rad}$).

5.2 Degrees of Freedom DOFs

The robotic manipulator's number of degrees of freedom is given by Grubler's formula:

$$DOF_G = m(N - 1 - J) + \sum_{i=1}^J f_i = 11 \quad (26)$$

where m is the maximum number of DOF in the space considered (6 in the 3D space), N is the number of bodies, including the ground (6 considering one spacecraft and five links), J is the number of joints of the robot (5 revolute joints) and f_i is the number of DOF provided by the single joint (1 for a revolute joint). Grubler's formula holds only if all joint constraints are independent, otherwise the formula provides a lower bound on the number of degrees of freedom.

The degrees of freedom of the entire multi-body system can be computed as follows:

$$DOF_{Tot} = DOF_{Base} + DOF_{Joints} = 11 \quad (27)$$

where DOF_{Base} is the number of DOFs of the base (6 in 3D space) and DOF_{Joints} is the sum of the internal DOFs provided by the joints (5 for 5 revolute joints).

An alternative way to evaluate the degrees of freedom (DOFs) of a multi-body system is to subtract from the DOFs of all the bodies involved the DOFs constrained by the joints:

$$DOF_{Tot} = mN - (m - f_i)J = 11 \quad (28)$$

where $(m - f_i)$ represent the number of DOFs constrained by the joints (5 DOFs constrained by a revolut joint).

The satellite-manipulator system can operate in three main control modes while the manipulator is controlled by its joint actuators:

1. Free-flying mode

The position of the base is controlled by actuators, and the attitude of the base is controlled by momentum exchange devices (e.g. reaction wheels or control moment gyroscopes). This mode is commonly used during large trajectory adjustments (e.g. the Hohmann transfer analysed in section 2) or for fine manoeuvres (e.g. close approach studied in section 3).

2. Attitude-controlled mode

The attitude is controlled by momentum exchange devices while the base's position is uncontrolled. This mode of operation focuses on stabilising or controlling orientation and is commonly used during in-orbit manipulation when stability and precision are needed.

3. Free-flying mode

Neither base position nor attitude is controlled. Since no active control is applied on position and orientation, this mode mainly relies on the conservation of angular momentum. This operative mode can be used during object capture or manipulations.

5.3 Mathematical formulation

To analyse a robotic manipulator, different mathematical approaches are needed. First of all, the kinematics of the multi-body system is described with a compact formulation. Successively, the propagation of the velocities is studied in order to derive the mathematical formulation needed to successively evaluate the propagation of the contact force along the robotic chain [4].

5.3.1 Kinematics

It is possible to uniquely describe the configuration of a multibody system by knowing the absolute position and orientation of the first body (or base, e.g. the spacecraft) and the relative position and orientation of all the other bodies (e.g. the link of the robotic manipulator) with respect to the base. The Homogeneous Transformation Matrix (HTM) ${}^{\mathcal{A}}T_{\mathcal{B}}$ can be used to univocally determine the pose (position and orientation) of a rigid body \mathcal{A} with respect to another rigid body \mathcal{B} :

$${}^{\mathcal{A}}T_{\mathcal{B}} \triangleq \begin{bmatrix} {}^{\mathcal{A}}\mathbf{R}_{\mathcal{B}} & {}^{o\mathcal{A}}\mathbf{r}_{o\mathcal{B}}^{\mathcal{A}} \\ \mathbf{0}_{1 \times 3} & \mathbf{I}_3 \end{bmatrix} \quad (29)$$

where ${}^{\mathcal{A}}\mathbf{R}_{\mathcal{B}}$ is the Direction Cosine Matrix (DCM) from CCS \mathcal{B} to CCS \mathcal{A} and ${}^{\mathcal{A}}\mathbf{r}_{o_{\mathcal{B}}}^{\mathcal{A}}$ the position vector from the origin of \mathcal{A} to the origin of \mathcal{B} . Please note that, unlike the DCM, which performs the change of coordinates of the same vector seen by two different CCS, the HTM performs the change of coordinates of the same point in two different coordinate systems. It is possible to concatenate successive homogeneous transformation (e.g. ${}^{\mathcal{A}}\mathbf{T}_{\mathcal{C}} = {}^{\mathcal{A}}\mathbf{T}_{\mathcal{B}} {}^{\mathcal{B}}\mathbf{T}_{\mathcal{C}}$). It is useful to solve the forward kinematics (or direct kinematics) problem, which involves determining the pose of one CCS relative to another within a multi-body system. This is equivalent to finding the HTM as a function of the kinematic properties (e.g. joint displacements) of the portion of the multi-body system between the two CCSs. To solve the direct kinematics problem, the joint displacement needs to be considered. In the considered cases, these are the angular rotations of the joints. By convention, the link i is preceded by the joint i and followed by the joint $i+1$; moreover, the joint-fixed CCS \mathcal{J}_i is rigidly connected to the joint-predecessor link CCS \mathcal{L}_{i-1} . Therefore, it is possible to consider two CCS on the same joint i , where the first one \mathcal{J}_i is rigidly connected to the previous link's CCS \mathcal{L}_{i-1} and the second one \mathcal{J}_i^+ is rigidly connected to the following link's CCS \mathcal{L}_i . By doing this, the HTM from the two links' CCS can be expressed as two constant HTMs and one HTM function of the joint displacement, as follows:

$${}^{\mathcal{L}_{i-1}}\mathbf{T}_{\mathcal{L}_i} = {}^{\mathcal{L}_{i-1}}\mathbf{T}_{\mathcal{J}_i} {}^{\mathcal{J}_i}\mathbf{T}_{\mathcal{L}_i} = {}^{\mathcal{L}_{i-1}}\mathbf{T}_{\mathcal{J}_i} {}^{\mathcal{J}_i}\mathbf{T}_{\mathcal{J}_i^+}(q_i) {}^{\mathcal{J}_i^+}\mathbf{T}_{\mathcal{L}_i} \quad (30)$$

where ${}^{\mathcal{L}_{i-1}}\mathbf{T}_{\mathcal{J}_i}$ and ${}^{\mathcal{J}_i^+}\mathbf{T}_{\mathcal{L}_i}$ are constant since \mathcal{J}_i is rigidly connected to \mathcal{L}_{i-1} and \mathcal{J}_i^+ is rigidly connected to \mathcal{L}_i , and ${}^{\mathcal{J}_i}\mathbf{T}_{\mathcal{J}_i^+}(q_i)$ is a function of the displacement of the joint i q_i .

In the considered scenario, there are only revolute joints, therefore, the displacement is an angular rotation $q_i = \theta_i$. The HTM of a revolute joint is described by the following formula:

$${}^{\mathcal{A}}\mathbf{T}_{\mathcal{B}} = \begin{bmatrix} {}^{\mathcal{A}}\mathbf{R}_{\mathcal{B}}(\hat{\mathbf{e}}_i, \theta_i) & \mathbf{0}_{3 \times 1} \\ \mathbf{0}_{1 \times 3} & I_3 \end{bmatrix} \quad (31)$$

where Euler's formula gives the rotation matrix:

$${}^{\mathcal{A}}\mathbf{R}_{\mathcal{B}}(\hat{\mathbf{e}}_i, \theta_i) = \cos(\theta_i)E_3 + [1 - \cos(\theta_i)]\hat{\mathbf{e}}_i\hat{\mathbf{e}}_i^T + \sin(\theta_i)\hat{\mathbf{e}}_i^\times \quad (32)$$

where E_3 is the identity matrix.

With this formulation, it is possible to determine the pose for each joint-fixed and link-fixed CCS.

5.3.2 Differential Kinematics

To assess the propagation of linear and angular velocities, it is necessary to introduce other mathematical quantities.

The Twist Propagation Matrix \mathbf{B}_{ij} from link \mathcal{L}_i to link \mathcal{L}_j is a 6×6 matrix defined as follows:

$$\mathbf{B}_{ij} \triangleq \begin{bmatrix} I_3 & \mathbf{0}_{3 \times 3} \\ \left(\mathbf{c}_{ij}^T\right)^\times & I_3 \end{bmatrix} \quad (33)$$

Where $(\mathbf{c}_{ij}^T)^\times$ is the vectorial product tensor of the vector \mathbf{c}_{ij}^T from the Centre of Mass (CoM) of the link j to the CoM of link i .

The Twist Propagation Matrix describes how the twist (combination of linear and angular velocities) propagates from link i to link j .

The Twist Propagation Vector from p_i link \mathcal{L}_j is a 6×1 matrix that encapsulates the velocity contributions based on the type of join. For revolute joints, the twist propagation vector includes both the joint axis and its cross-product with the vector g_{i+1} , representing the displacement from the joint to the next link. It is defined as follows:

$$p_i \triangleq \begin{bmatrix} \hat{\mathbf{e}}_i^T \\ (\hat{\mathbf{e}}_i^T)^\times \mathbf{g}_i^T \end{bmatrix} \quad (34)$$

The Velocity Transformation Matrix (or System Jacobian Matrix) maps joint-space velocities to the twists of all links. It is defined as:

$$\mathbf{N} = \mathbf{N}_l \mathbf{N}_d \quad (35)$$

where:

- \mathbf{N}_l is a square block-lower-triangular matrix of size $6(n+1) \times 6(n+1)$, defined as follows:

$$\mathbf{N}_l \triangleq \begin{bmatrix} \mathbf{I}_6 & \mathbf{0}_{6 \times 6} & \cdots & \mathbf{0}_{6 \times 6} \\ \mathbf{B}_{10} & \mathbf{I}_6 & \cdots & \mathbf{0}_{6 \times 6} \\ \vdots & \vdots & \ddots & \vdots \\ \mathbf{B}_{n0} & \mathbf{B}_{n1} & \cdots & \mathbf{I}_6 \end{bmatrix} \quad (36)$$

where the \mathbf{B}_{ij} matrices are defined according to Equation 33.

- \mathbf{N}_d is a rectangular block-diagonal matrix of size $6(n+1) \times (6+n)$, defined as follows:

$$\mathbf{N}_d \triangleq \begin{bmatrix} \mathbf{P}_0 & \mathbf{0}_{6 \times 1} & \cdots & \mathbf{0}_{6 \times 1} \\ \mathbf{0}_{6 \times 6} & \mathbf{p}_1 & \cdots & \mathbf{0}_{6 \times 1} \\ \vdots & \vdots & \ddots & \vdots \\ \mathbf{0}_{6 \times 6} & \mathbf{0}_{6 \times 1} & \cdots & \mathbf{p}_n \end{bmatrix} \quad (37)$$

where \mathbf{P}_0 is the Base Transformation Matrix and is equal to the identity \mathbf{I}_6 since $\boldsymbol{\omega}_0 = \boldsymbol{\omega}_0^T$, and p_i are defined according to Equation 34.

The System Jacobian Matrix is used in the System Direct Differential Kinematic equation to efficiently map the velocities from joint space (angular and linear velocities of the base and joints) to the operational space (generalised twist matrix):

$$\mathbf{t} = \mathbf{N} \mathbf{u} \quad (38)$$

where:

- $\mathbf{t} \in \mathbb{R}^{6(n+1)}$ Generalised Twist Matrix — represents the velocities of all links in operational space.
- $\mathbf{u} \in \mathbb{R}^{6+n}$ Generalised Velocity Matrix — includes angular and linear velocities of the base link and the joint velocities.
- $\mathbf{N} \in \mathbb{R}^{6(n+1) \times (6+n)}$ Velocity Transformation Matrix (or System Jacobian Matrix) — maps joint-space velocities to the twists of all links.

5.3.3 Dynamics

To assess the propagation of the contact force caused by the capture of the debris along the robotic arm, the generalised force (or joint-space force) matrix $\boldsymbol{\tau}$ is computed. It represents the mapping of operational-space wrenches to the joint space. Therefore, the system-level implicit equation of motion in the joint space is solved:

$$\boldsymbol{\tau} \triangleq \mathbf{N}^\top \mathbf{w} = \begin{bmatrix} \boldsymbol{\tau}_0 \\ \boldsymbol{\tau}_m \end{bmatrix} \quad (39)$$

where \mathbf{N}^\top is the transpose of the System Jacobian Matrix (as computed in Equation 35) and $\mathbf{w} \in \mathbb{R}^{6(n+1)}$ is the Generalised (system) wrench column matrix, representing the collection of external forces and moments on all links. It considers all the resultant external moments and forces applied to the CoM of each link. Therefore, it represents the actions in the operational space.

The generalised force matrix $\boldsymbol{\tau}$ can be further divided into two components, $\boldsymbol{\tau}_0$ and $\boldsymbol{\tau}_m$, which represents, respectively, the base-link generalised forces, and the manipulator's generalised forces (each i -th component of $\boldsymbol{\tau}_m$ corresponds to the actuating force or torque at the i -th joint of the manipulator).

5.4 Numerical Implementation

The propagation of the contact force caused by the capture of the debris along the robotic arm is computed following the procedures presented in subsection 5.3. The robotic arm geometrical properties are reported in Table 2 in subsection 5.1. For this simplified analysis, it is considered an in-plane motion, following the consideration stated in subsection 5.1. Therefore, the angular displacement of the joints \mathcal{J}_1 , \mathcal{J}_3 and \mathcal{J}_5 are null ($\theta_1 = \theta_3 = \theta_5 = 0$ rad), while the remaining joints rotate of an equal angle: $\theta_2 = \theta_4 = 45^\circ$. The contact force is assumed to be $F = 20$ N, within the range of contact forces for space debris capture available in the literature [13]. For the sake of simplicity, the contact force is assumed to be directed toward the end effector and parallel to the final link. Therefore, the wrench \mathbf{w}_5 of the link \mathcal{L}_5 can be written as: $\mathbf{w}_5 = [0 \ 0 \ 0 \ 0 \ -F \ 0]^\top$. No other external forces or torques are applied on the CoMs of other links.

The geometrical position of the joints' Centres of Mass (CoMs) is computed according to the considered geometry. The vectors \underline{g} connecting the centre of each joint \mathcal{J} to the CoM of the successive link \mathcal{L} are evaluated according to the angular displacement of \mathcal{J}_2 and \mathcal{J}_4 . Then they are used to evaluate the position $\underline{r}_i^{\mathcal{I}}$ of the link \mathcal{L}_i in the inertial reference frame, starting from the position of the base $\underline{r}_0^{\mathcal{I}}$ and going forward through the robotic arm. Please note that the origin of the inertial reference frame is centred in the base centre of mass ($\underline{r}_0^{\mathcal{I}} = 0$) and the base is approximated as a cube of edges long 1 m. Each joint's versor is defined as a function of the angular displacement of the other joints, when needed.

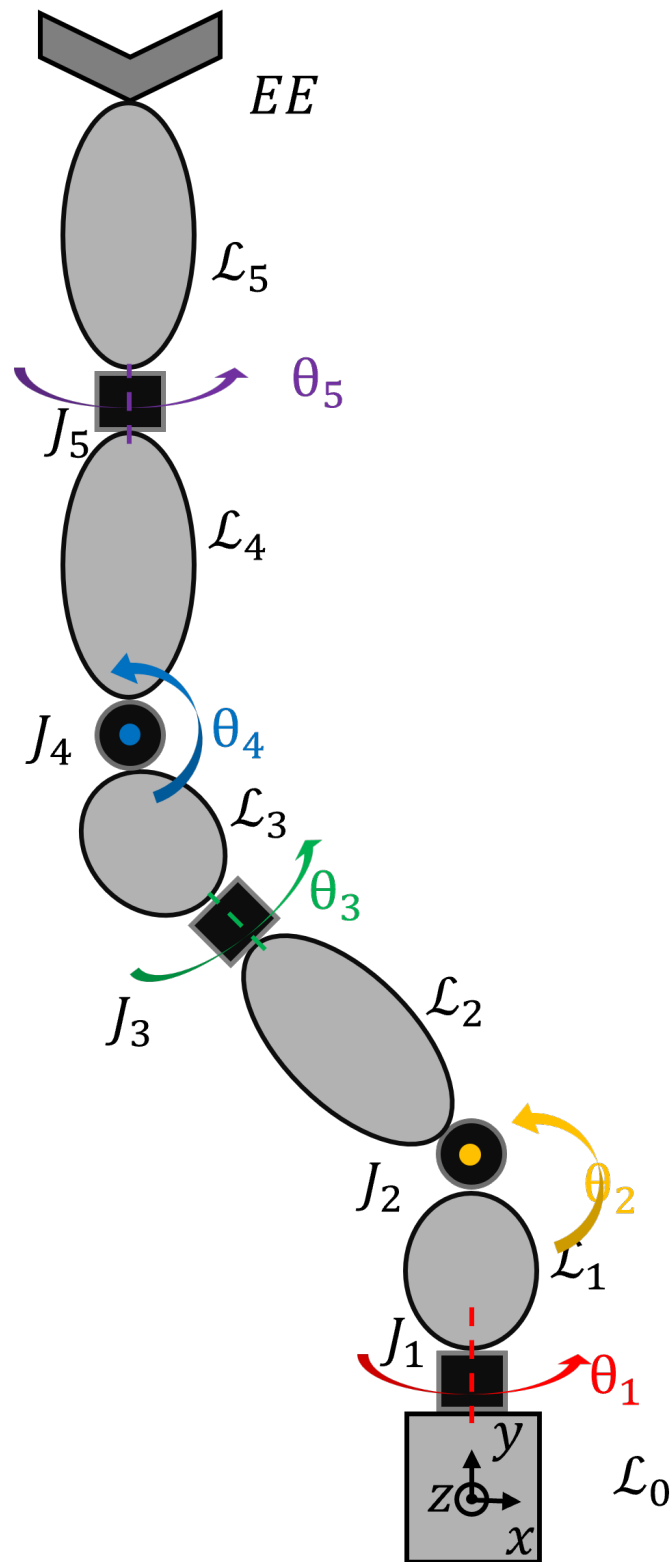


Figure 14: Schematic representation of the robotic manipulator in a 2D configuration where the joints J_1 , J_3 and J_5 are fixed.

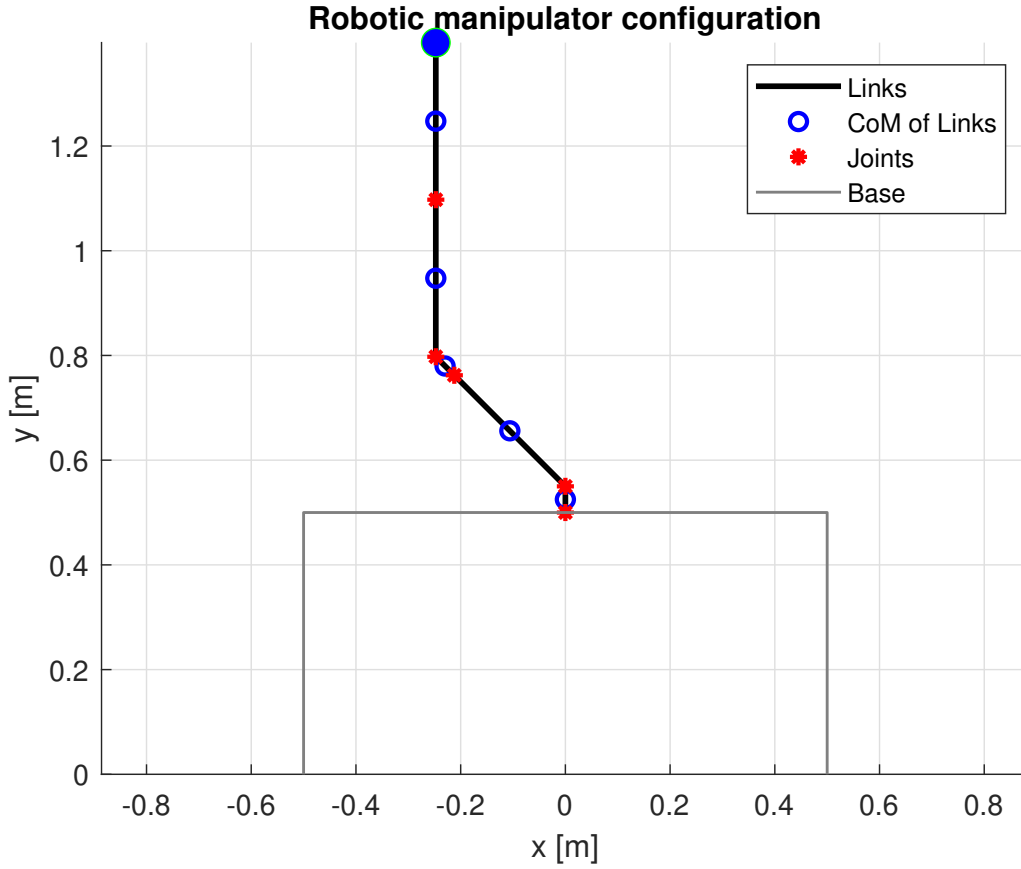


Figure 15: Manipulator in the first configuration with $\theta_2 = -45^\circ$ and $\theta_4 = -45^\circ$ and $F = 20$ N applied along the y direction.

The computation of the System Jacobian Matrix \mathbf{N} , according to Equation 35 is performed. Twist Propagation Matrices \mathbf{B}_{ij} are computed according to Equation 33 to assemble the \mathbf{N}_l matrix (see Equation 36), and the Twist Propagation Vectors p_i are computed according to Equation 34 to assemble the \mathbf{N}_d matrix (see Equation 37).

Finally, the generalised force matrix $\boldsymbol{\tau}$ is computed according to Equation 39.

Figure 15 shows the configuration of the manipulator discussed above, with $\theta_2 = -45^\circ$ and $\theta_4 = -45^\circ$ and $F = 20$ N applied along the y direction. The results of the first configuration are reported in

Table 3: Torques and forces on the base and joints for case 1.

Case	F_{Bx} [N]	F_{By} [N]	T_B [Nm]	$T_{J\in}$ [Nm]	$T_{J\Delta}$ [Nm]
Case 1	0.00	-20.00	4.95	4.95	0.00

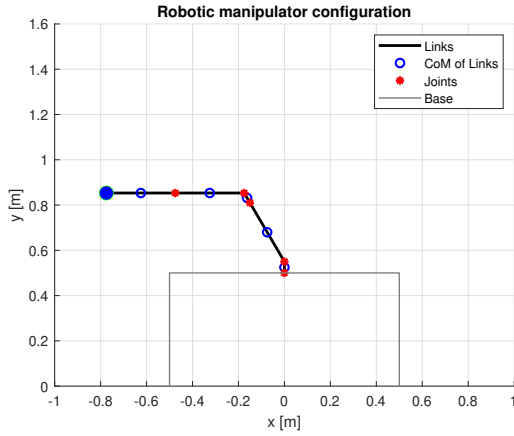
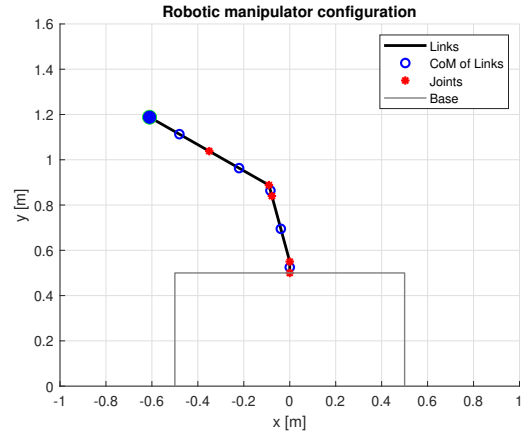
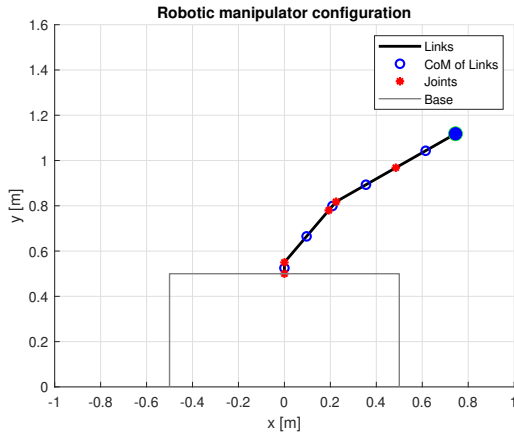
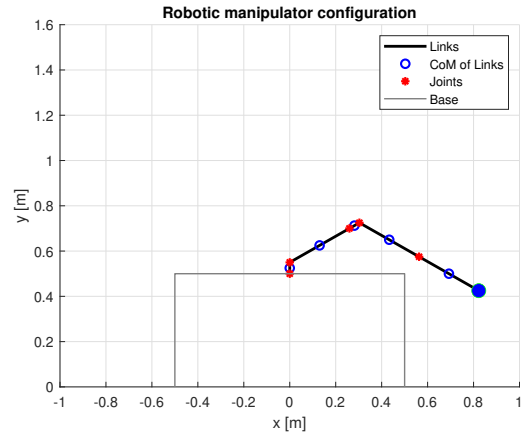
(a) Case 2 - $\theta_2 = -30^\circ$ and $\theta_4 = -60^\circ$ (b) Case 3 - $\theta_2 = -15^\circ$ and $\theta_4 = -45^\circ$ (c) Case 4 - $\theta_2 = 40^\circ$ and $\theta_4 = 20^\circ$ (d) Case 5 - $\theta_2 = 60^\circ$ and $\theta_4 = 60^\circ$

Figure 16: 4 different configurations of the robotic manipulator with different angular displacement of the joints \mathcal{J}_2 and \mathcal{J}_5 under the same force ($F = -20\text{N}$).

Figure 16 shows 4 configurations studied to assess how the propagation of the force changes with different angular displacements of the joints. The configurations considered are:

- Case 2 - $\theta_2 = -30^\circ$ and $\theta_4 = -60^\circ$, shown in Figure 16a.
- Case 3 - $\theta_2 = -15^\circ$ and $\theta_4 = -45^\circ$, shown in Figure 16b.
- Case 4 - $\theta_2 = 40^\circ$ and $\theta_4 = 20^\circ$, shown in Figure 16c.
- Case 5 - $\theta_2 = 60^\circ$ and $\theta_4 = 60^\circ$, shown in Figure 16d.

The results of the comparison between the different cases are highlighted in Table 4.

Table 4: Torques and forces on the base and joints for cases 2,3, 4, and 5.

Case	F_{Bx} [N]	F_{By} [N]	T_B [Nm]	$T_{\mathcal{J}_\epsilon}$ [Nm]	$T_{\mathcal{J}_\Delta}$ [Nm]
Case 2	0.00	-20.00	12.50	12.50	9.00
Case 3	0.00	-20.00	9.61	9.61	7.79
Case 4	0.00	-20.00	-12.29	-12.29	-7.79
Case 5	0.00	-20.00	-13.86	-13.86	-7.79

6 Impulse optimisation problem for the perturbed rendezvous

This section aims to evaluate the required ΔV necessary to complete the rendezvous with the chaser affected by the aforementioned drag perturbation.

6.1 Preliminary considerations, fixed ToF

This subsection aims to present some observations made while approaching this task, providing context for the first version of the solution given in the next subsection. The time of flight (ToF), which was optimised for the unperturbed rendezvous, is taken as a "design parameter"; thus, it is fixed in order to reduce the degrees of freedom. Drag is assumed to be a small perturbation (this assumption can be confronted with the previous results), therefore, a solution should be searched in a certain range of the impulse derived from the ideal case. The numerical propagation can be seen as a black box which takes as input parameters the two components of the first impulse (the motion is in a plane); the chaser at the end of the rendezvous should be, within a tolerance range, at the origin of the target Hill CCS, hence 2 "constrained" output parameters are considered (ξ and η); the solution is, therefore, supposed to be unique. In order to test this observation, a numerical computation of the 2 position parameters associated with various impulses is performed.

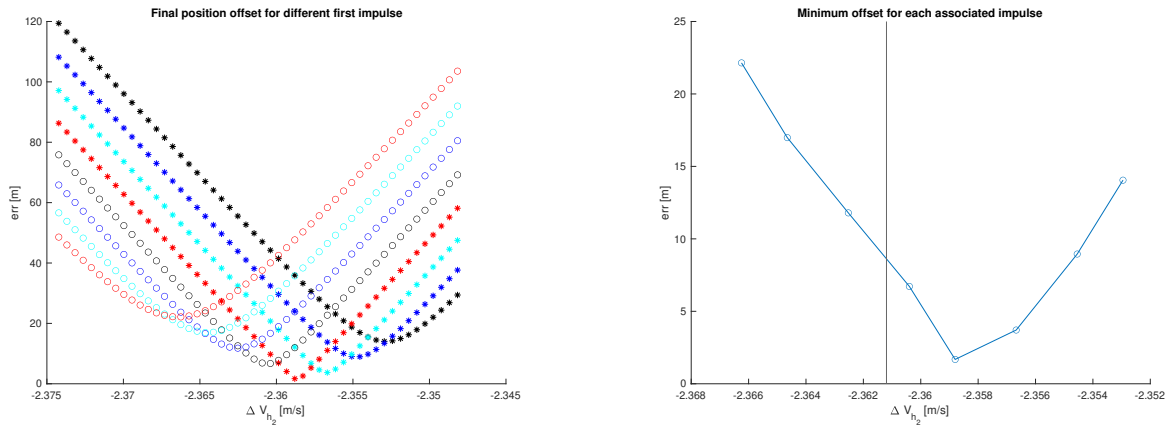


Figure 17: The first graph shows final position offsets (err) for different values of impulse (the second component is on the x axis while the first component is associated with the symbol used). The second graph collects the minima of each branch, the vertical line corresponds to the value of the second component of the unperturbed impulse.

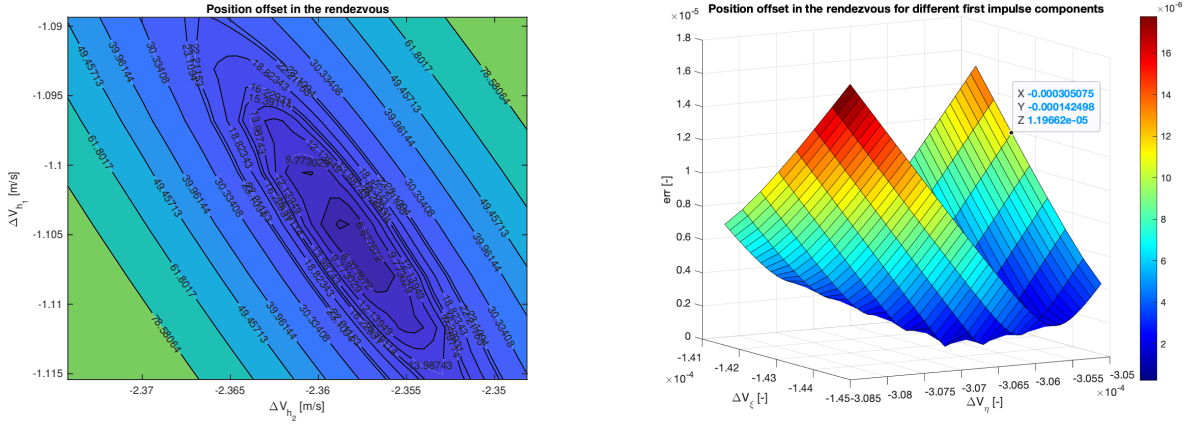


Figure 18: These two graphs are two possible ways to visualise the final position offset (err) for different impulse components. It can be seen how the plots seem to confirm the hypothesis of a unique solution in terms of impulse for a perturbed rendezvous. It is to be noted that each colored area in the contour graph is associated with a value of err in meters.

6.2 First version of the solution, fixed ToF

This first version of the solution was written leveraging the observations made in the previous subsection. This is an iterative method that calculates some solutions for various impulses in the intended range; at the end of each iteration, the absolute minimum of the position offset is saved along with its associated impulse. The cycle is controlled in order to have a monotonic decreasing offset, avoiding losing the solution from the investigated range: if one iteration does not get closer to the solution, the value is not saved, and the process is repeated, trying a larger number of impulses. After an accepted iteration, the range is reduced, and the reference impulse is the one from the previous cycle. The process ends when a maximum iteration is reached or it is obtained a final position offset smaller than a chosen reference value (in this case, $1\mu\text{m}$). In the end, an integration is repeated in order to check the result. The second impulse is used to nullify the relative velocity with respect to the target, thus, it is the opposite of the final velocity components calculated with the last numerical propagation. In this case, the final position offset is $0.745\mu\text{m}$, this value, smaller than the chosen threshold, was achieved after 29 accepted iterations. The new total impulse needed is $2.8313 \frac{m}{s}$.

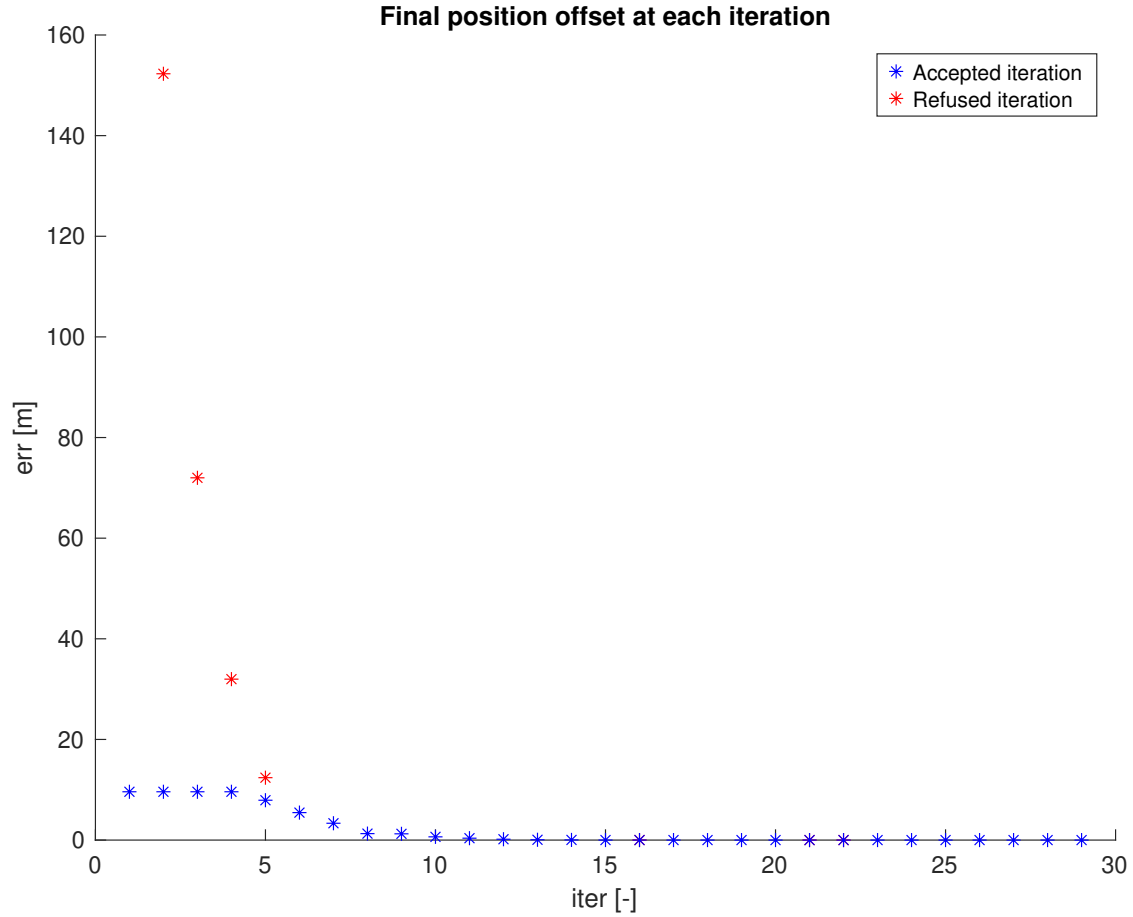


Figure 19: Final position offset behaviour at each iteration.

6.3 Second version of the solution, fixed ToF

In this subsection, a different, more compact, possible solution is presented; it partially leverages the previous observations. It is employed the MATLAB function *fsolve* is employed in order to find a zero of a "position error function" (called *pos_err*) which calculates ξ and η (of course, they both need to be equal to 0). The parameter that varies inside the *fsolve* function is the impulse (2 components) that is summed to the initial offset in velocity. For the first try, the first guess for *fsolve* is the value of the impulse calculated in the unperturbed rendezvous. The output of *fsolve* is the impulse needed to achieve a rendezvous in the perturbed condition, it is finally verified with a last numerical propagation. The second impulse is the opposite of the velocity values found at the end of the numerical propagation. In this case, the final position offset is $3.213 \mu\text{m}$. The new total impulse needed is $2.8313 \frac{\text{m}}{\text{s}}$. These results can be considered in accordance with the first method presented.

6.4 Third version of the solution, variable ToF

In this proposed version of the solution, the time of flight is not fixed. The approach used in subsection 6.3 implementing *fsolve* is integrated in a cycle that selects, at each iteration, a possible time of flight from a vector. Only results where the final position offset is below a chosen threshold are accepted (in this case, $10\ \mu\text{m}$); it should be noted that in the graph of the various total impulses for the corresponding ToF, accepted iterations are shown with a blue dot mark (Figure 20). The vector containing the ToFs is created using the *linspace* function; it is fundamental to use an appropriate combination of range and number of points in order to avoid obtaining a worse solution compared to the other versions. After the cycle is completed it is chosen the minimum total impulse with its associated time of flight is chosen. It is now possible to compare this result with the one obtained in subsection 6.3. It is interesting to notice how the total impulse is just barely smaller, this validates the sensibleness of the decision made in the previous versions to keep the ToF fixed as a design parameter (unperturbed optimised ToF=2199.1140 s). The perturbed rendezvous is achieved in 2215.6073 s, using a total impulse of $2.8312\ \frac{\text{m}}{\text{s}}$. This impulse is 99.997572% of the one calculated with fixed ToF.

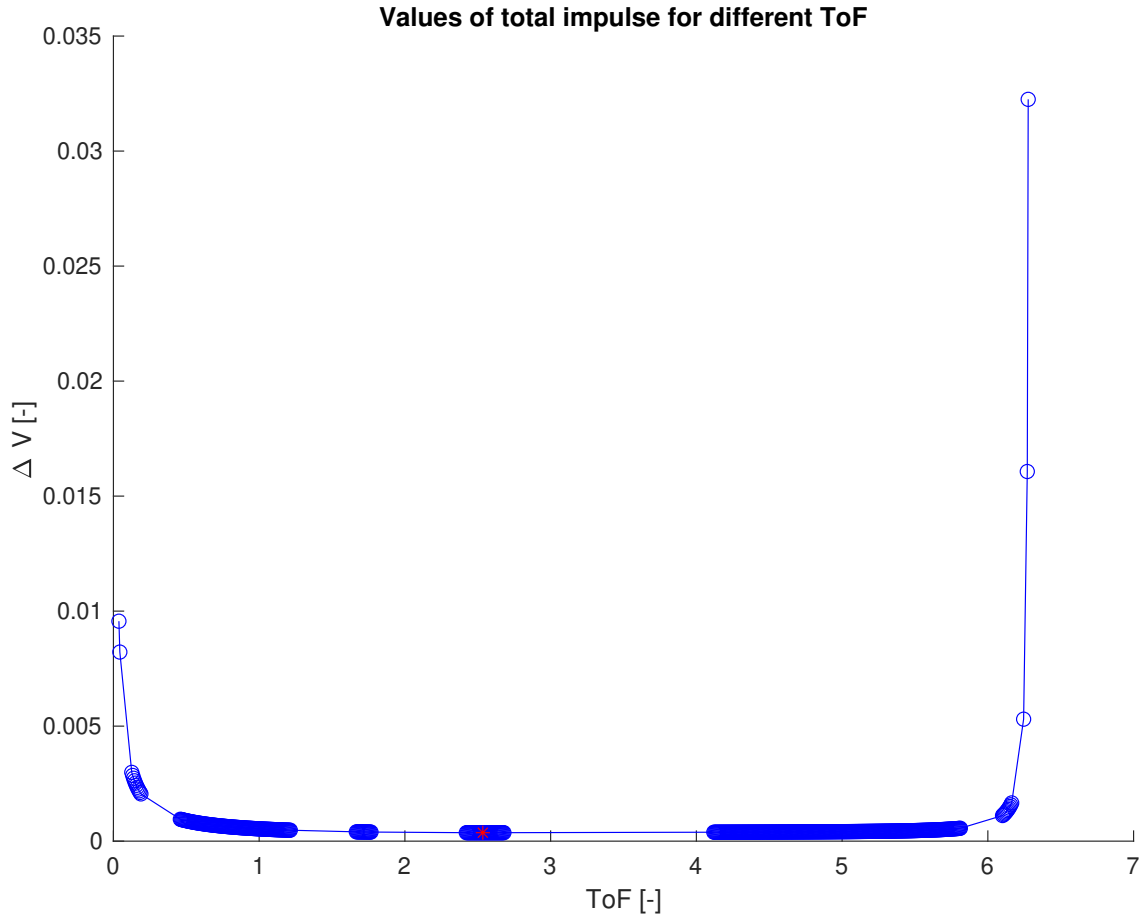


Figure 20: Each blue circle corresponds to an accepted iteration, the red star is the minimum total impulse needed to achieve a perturbed rendezvous.

7 Space debris retrieval and de-orbiting technologies

In recent years, the increasing amount of space debris has raised concerns about the safety and long-term sustainability of orbital environments. Objects such as defunct satellites, upper rocket stages, and fragments from collisions or explosions continue to orbit Earth, posing collision risks to operational assets. In Table 5, the estimated debris population is reported.

Table 5: Number and dimension of debris estimated based on statistical model, last update 31 March 2025, ESA [14]

Category	Dimension	Number
Large	greater than 10 cm	54 000
Medium	from greater than 1 cm to 10 cm	1 200 000
Small	from greater than 1 mm to 1 cm	140 000 000

To address this challenge, many space debris capture, retrieval and de-orbiting technologies have been proposed, each with different levels of technological feasibility and applicability. These technologies aim to either capture and retrieve debris or induce its re-entry into Earth's atmosphere in a controlled or passive manner. A typical ADR mission usually follows similar steps: launch of the active spacecraft, rendezvous with the debris target, evaluation of the motion and mass-geometric characteristics, de-tumbling (if necessary), docking manoeuvre or capture, active transportation, re-entry or separation of the active spacecraft from the debris and rendezvous with other targets. Depending on the mission scenario, one phase can change.

ADR methods have been classified in many ways according to different studies: Shan, Guo, and Gill [15] focus on different capturing (tentacles, single/multiple robotic arm, net capturing, tether gripper and harpoon) and removal (drag augmentation system, ElcetroDynamic Tethers, contactless removal) methods. Mark and Kamath [16] classify methods in collective, laser-based, ion-beam shepherd-based, tether-based, sail-based, satellite-based, unconventional and dynamical systems-based. Ledkov and Aslanov [17] analyse contact and contactless approaches.

In the considered case study, the capture is performed through the robotic manipulator. Therefore, a proper technology to deorbit the satellite and the debris should be evaluated.

7.1 Deorbiting technologies trade-off

A successful ADR solution must consider the debris size, tumbling motion, orbit type, technological readiness of the system, cost of the mission, risks and many other factors. A simple and qualitative trade-off to understand which deorbiting method could be the most suitable is performed based on 5 main parameters:

1. Technology Readiness Level (TRL) - To quantify the technological maturity of the system on a scale from 1 (basic research) to 9 (system tested in operational environment)
2. Scalability (S) - The system is capable of deorbiting debris of different dimensions with minor changes in the system configuration
3. Flexibility (F) - The system can perform deorbiting in different environments (e.g. different orbital altitudes or inclinations)

4. Cost (C) - Cost-effectiveness of the method
5. Susceptibility to debris impact (D) - Low vulnerability of the ADR system to being damaged or disrupted by collisions with space debris

Each parameter is quantified on a scale from 0 to 1 (e.g. 0.8 debris susceptibility means that the system is not very sensitive to debris impact) except for TRL (scale from 1 to 9). The choice of these values is based on the consideration of these technologies available in the literature [15, 16, 17]. The most suitable method is chosen according to the following equation:

$$R = w_{TRL}TRL + w_SS + w_FF + w_CC + w_DD \quad (40)$$

where the w_i are the weights to consider the different relevance of the parameters; for an ADR mission, debris susceptibility and cost are particularly relevant. One of the main complexities of this kind of mission is to avoid producing more debris, therefore, the system should be able to resist impact with small debris as much as possible. Moreover, the cost-effectiveness of the mission is fundamental; since neither scientific nor economic output is generated by the mission, it's difficult to find financial support. The weights are chosen such that $0 \leq R \leq 1$. The deorbiting method with the highest value of R is the most suitable for this mission case study.

Among all the possible solutions, three deorbiting methods are considered: thrusters, ElectroDynamic Tethers (EDT) and solar sails.

7.1.1 Thrusters

Thrusters are the most common propulsive system in space. They can be used for a multitude of purposes and are a very well-established technology. The most straightforward solution to easily deorbit space debris is to capture it (e.g. with a robotic manipulator) and use a thruster to perform a controlled re-entry.

Clearspace-1 is ESA's first ADR mission led by Swiss startup ClaeSpace [18]. The mission aims to demonstrate technologies for rendezvous, capture, and deorbit and to remove an uncooperative object from orbit. According to plans, once the target is captured with robotic tentacles, the spacecraft will perform a set of de-orbit burns to ensure the re-entry.

However, there are some drawbacks related to the usage of thrusters for deorbiting space debris. The most important one is that they are not cost-effective considering their need for fuel. The economic constraints are the most stringent for ADR missions, considering that they don't produce any scientific or economic results, and therefore, they need to be as cheap as possible.

7.1.2 Solar sail

The solar sail is made from lightweight reflective material and uses solar radiation pressure to generate force Figure 21. To date, orbital experiments have been carried out, like Japan's IKAROS [19] or the LightSail-2 project [20]. Solar sails can be used as a propellant-less device to deorbit a payload from Earth orbit, to produce a continuous net force lowering the debris' orbit. However, even if solar sails have been tested in a relevant space environment, they have never been validated to deorbit a payload from Earth orbit. Therefore, their TRL for the deorbiting mission is not considered to be as high as that of thrusters and EDT.

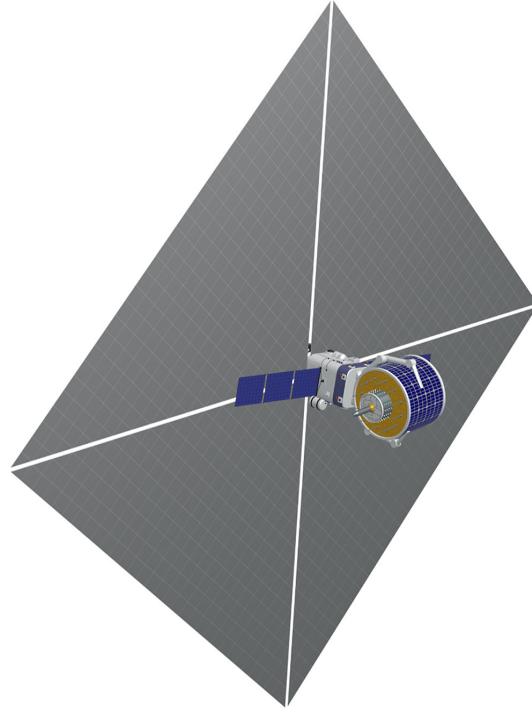


Figure 21: Schematic of solar sail application for deorbiting a piece of space debris [17].

With respect to thrusters, solar sails need almost no fuel, making them a valuable solution for cost-effective ADR missions. However, since the solar radiation pressure is very low, they need very large surfaces of reflective material. This can pose a significant risk for debris collision.

7.1.3 ElectroDynamic Tether

ElectroDynamic Tethers (EDTs) consist of a conductive tether connecting the two bodies (e.g. the spacecraft and the debris) that can generate forces along the tether thanks to the interaction of the tether with Earth's magnetic field and the space environment. It employs the electromagnetic induction between a circuit moving through a magnetic field, inducing an electromotive force (EMF) in the wire. In an EDT system, as the tether orbits Earth, it moves through the planet's geomagnetic field, cutting across magnetic field lines and inducing an EMF. It generates a potential difference between the two ends of the tether, with the upper end becoming positively charged relative to the lower end. To produce an electric current flow, the circuit must be closed. Plasma contactors positioned at the end of the tether establish electrical contact with Earth's plasma environment, forming a current loop (so-called "phantom loop") which flows through the tether, the surrounding plasma and the ionosphere. The positively charged upper end of the tether collects electrons from the ambient plasma, forming a net-positive charge cloud, while the negatively charged lower end emits electrons, generating a net-negative cloud. Alternative methods for producing current flow include non-insulated bare tethers (e.g. the one used during KITE mission in 2016 [21]), where the tether itself collects electrons, or Low Work function Tethers (LWT), which can both collect and emit electrons thanks to a specific coating that allows the photoelectron emission of the tether itself under solar illumination. This creates a photocathode, which emits electrons, enabling the flow of the current. This technology is extremely promising for deorbiting applications and will be tested in orbit in mid-2026 during the E.T.PACK mission [22, 23].

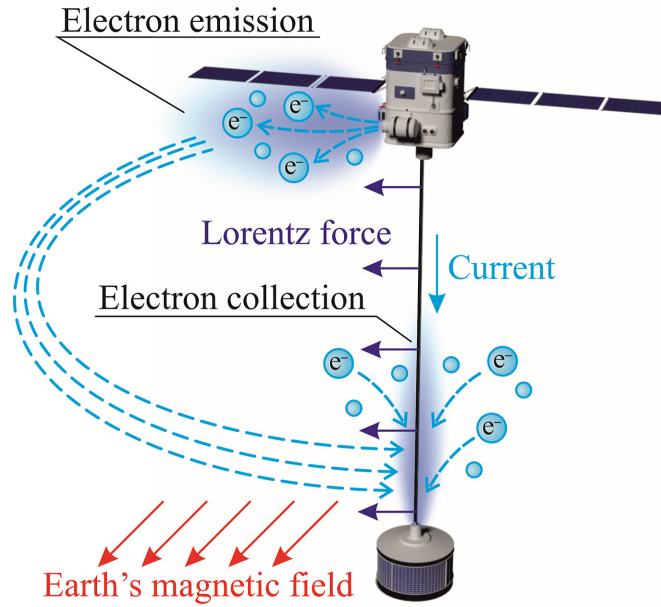


Figure 22: Schmatic representation of the forces acting on an ElectroDynamic Tether [17].

Depending on the direction of the electric current, an EDT can produce either thrust or drag. When the current is naturally induced by motion through the magnetic field, the resulting drag force acts to reduce the system's velocity, gradually lowering the orbital altitude of the system. EDT systems, in principle, require no propellant, making them lightweight and cost-efficient.

However, the drag force produced by this system is highly dependent on the interaction between the tether and the magnetic field lines. Therefore, this system is highly inefficient in high-altitude and high-inclination orbits.

ElectroDynamic Tethers have been tested under different conditions throughout the years during more than 20 missions [24], with PMG [25] mission being the first in-orbit demonstration in 1993 or more recently by TEPCE [26] in 2019.

7.2 Results of the trade-off

A trade-off analysis between the three deorbiting technologies presented in subsection 7.1.1, 7.1.2, and 7.1.3 is conducted according to the parameters discussed in subsection 7.1. The results are highlighted in Table 6, where the *Results* are computed according to Equation 40.

Table 6: Trade-off between three different deorbiting methods. According to the results of this analysis, the ElectroDynamic Tether (EDT) is the most suitable deorbit method for the considered case study.

ADR removal method	TRL	Scalability	Flexibility	Cost	Debris susceptibility	Result
EDT	9	0.7	0.4	0.8	0.8	0.73
Solar sail	8	0.4	0.7	0.7	0.1	0.51
Thrusters	9	1	1	0.1	0.5	0.58

The ElectroDynamic Tether is preferred as a deorbiting device for the considered case study. This tech-

nology is highly efficient in the considered orbital condition (low-altitude equatorial orbit), moreover, it is cost-effective with respect to the thruster solution and is highly resistant to debris impact with respect to the solar sail, thanks to the innovative tether structural configuration developed in recent years [27, 28].

7.3 ElectroDynamic Tether for debris removal in the considered case study

ElectroDynamic Tethers are a compact, simple and cost-effective solution to deorbit a payload. This system simply encompasses a conductive tether deployed from the main spacecraft and an end mass, which can be the captured debris.

One interesting scenario could be to consider a multiple-debris ADR mission, in which the main spacecraft visits more debris, rendezvous and docks with each of them, and connects them with EDT devices thanks to the robotic arm. This mission can be quite complex from an astrodynamics and space logistics point of view, since the multiple targets would probably be in different orbits, with different altitudes, inclinations, and RAANs. In a real-case scenario, an optimisation problem to assess the best trajectory would be needed.

In the considered case study, the spacecraft is capable of performing the capture of the debris thanks to a robotic manipulator. Once the capture phase is completed, the EDT device could be attached to the debris. Then the main spacecraft would release the debris and perform the successive rendezvous.

On the debris, the EDT device could autonomously deploy the tether and successively stabilise in a vertical configuration thanks to the gravity gradient torque. The EDT would then perform a completely passive deorbiting phase thanks to the drag force generated by the interaction with the magnetic field.

A compact EDT device, called Terminator Tape, has been tested during three missions between 2019 and 2020, named PROX-1, NPSAT-1 [29] and Dragracer [30], with the objective of demonstrating the capability of deorbiting a payload with a compact and passive module. These three missions successfully demonstrated the capability of this small device to deorbit the payload.

In the proposed mission scenario, the main spacecraft is considered able to dock and capture the debris. In real cases, this is the most complex part that sets the most stringent requirements and determines complex dynamics. If this phase is assumed to be completed by the spacecraft, it should be relatively easy to attach a passive EDT module (similar to the Terminator Tape) to the debris to deorbit it autonomously.

One of the main advantages of this mission scenario is the capability of visiting multiple targets, thus performing more removal in the same mission. It can be highly expensive in terms of fuel consumption, but highly rewarding in terms of debris mitigation.

Moreover, the spacecraft itself has only one more requirement with respect to the ones it would have without the ADR mission, which is the capability of connecting the debris with the EDT module. Since the debris will successively deorbit autonomously, the dynamic of the spacecraft is not further affected by the debris.

8 Conclusion

To conclude, in this work, a space debris removal mission is modelled. The objective of the study is to take into account all the phases of a space debris removal mission, from the transfer to the relative approach, considering also a simplified model for the capture.

In section 2, the Hohmann transfer, which is the orbital transfer with minimum Δv between the chaser's and the target's orbit, is studied. The required Δv , the Time of Flight (ToF) and the phasing angle and time are analytically computed. Successively, the equations of motion of the Kepler Restricted 2-Body Problem are numerically integrated. The comparison between the analytical and the numerical results demonstrated the good approximation of the numerical propagation.

In section 3, the relative dynamic between the chaser and the target is studied under the simplified hypothesis of the Hill-Chloessy-Whiltshire (HCW) equations. The HCW are solved using both the analytical formulation and the numerical integration. Moreover, the minimum impulse and the associated ToF are derived. Finally, the numerical results are compared with the analytical ones, showing that the HCW equations, in the considered scenario, are a good approximation.

In section 4 the effect of the drag perturbation of the residual atmosphere is evaluated, highlighting how the final approach of the chaser would miss the target.

A simplified model to study the propagation of the contact force caused by the capture of the debris along the robotic manipulator is presented in section 5. The robotic arm is designed and modelled with a rigorous mathematical approach. The propagation of the contact force is computed numerically studying different configurations of the manipulator to consider the effect of the angular displacement of the joints.

In section 6, a method to calculate the impulse necessary to achieve a rendezvous in the perturbed condition is studied. It is presented at first as a possible solution with ToF fixed as a design parameter; in the final solution, the impulse is optimised considering different possible ToFs.

Some Active Debris Removal technologies are reviewed in section 7, to assess which one could be the most suitable for the scenario considered. An ElectroDynamic Tether is selected as a result of a trade-off analysis as the most suitable deorbiting technology for the mission scenario analysed.

References

- [1] Walter Hohmann. *The Attainability of Heavenly Bodies*. NASA Technical Translation F-44, 1960 (cit. on p. 6).
- [2] Howard D. Curtis. “Chapter 6 - Orbital maneuvers”. In: *Orbital Mechanics for Engineering Students (Fourth Edition)*. Ed. by Howard D. Curtis. Fourth Edition. Aerospace Engineering. Butterworth-Heinemann, 2021, pp. 287–350. ISBN: 978-0-12-824025-0. DOI: <https://doi.org/10.1016/B978-0-12-824025-0.00006-4>. URL: <https://www.sciencedirect.com/science/article/pii/B9780128240250000064> (cit. on p. 6).
- [3] Wikipedia. *Hohmann transfer orbit*. URL: https://en.wikipedia.org/wiki/Hohmann_transfer_orbit?utm_source=chatgpt.com (visited on 05/11/2025) (cit. on p. 6).
- [4] Politecnico di Torino. *Orbital Robotics and Distributed Space Systems Class Notes*. 2025 (cit. on pp. 7, 8, 13, 25).
- [5] W. H. CLOHESSY and R. S. WILTSHIRE. “Terminal Guidance System for Satellite Rendezvous”. In: *Journal of the Aerospace Sciences* 27.9 (1960), pp. 653–658. DOI: [10.2514/8.8704](https://doi.org/10.2514/8.8704). eprint: <https://doi.org/10.2514/8.8704>. URL: <https://doi.org/10.2514/8.8704> (cit. on p. 13).
- [6] United States Committee on Extension to the Standard Atmosphere. *U.S. Standard Atmosphere, 1976*. Washington, D.C., 1976 (cit. on p. 18).
- [7] Haibin Yin, Shansheng Huang, Mingchang He, and Junfeng Li. “A unified design for lightweight robotic arms based on unified description of structure and drive trains”. In: *International Journal of Advanced Robotic Systems* 14.4 (2017), p. 1729881417716383. DOI: [10.1177/1729881417716383](https://doi.org/10.1177/1729881417716383). eprint: <https://doi.org/10.1177/1729881417716383>. URL: <https://doi.org/10.1177/1729881417716383> (cit. on p. 23).
- [8] M. Oda, K. Kibe, and F. Yamagata. “ETS-VII, space robot in-orbit experiment satellite”. In: *Proceedings of IEEE International Conference on Robotics and Automation*. Vol. 1. Apr. 1996, 739–744 vol.1. DOI: [10.1109/ROBOT.1996.503862](https://doi.org/10.1109/ROBOT.1996.503862) (cit. on p. 23).
- [9] Mitsushige Oda et al. “ETS-VII: achievements, troubles and future”. In: *Proceedings of the 6th International Symposium on Artificial Intelligence and Robotics & Automation in Space: ISAIRAS 2001*. 2001 (cit. on p. 23).
- [10] Robert B. Friend. “Orbital Express program summary and mission overview”. In: *Sensors and Systems for Space Applications II*. Ed. by Richard T. Howard and Pejmun Motaghedi. Vol. 6958. SPIE, 2008, p. 695803. DOI: [10.1117/12.783792](https://doi.org/10.1117/12.783792). URL: <https://doi.org/10.1117/12.783792> (cit. on p. 23).
- [11] DLR Institute of Robotics and Mechatronics. *LWR III*. URL: https://www.dlr.de/en/rm/research/robotic-systems/arms/lwr-iii?utm_source=chatgpt.com (visited on 05/31/2025) (cit. on p. 23).
- [12] DLR Institute of Robotics and Mechatronics. *ROKVISS*. URL: https://www.dlr.de/en/rm/research/robotic-systems/arms/rokviss?utm_source=chatgpt.com (visited on 05/31/2025) (cit. on p. 23).
- [13] Melanie A. Orzechowski and Michael C. F. Bazzocchi. “Multicriteria Analysis of Robotic End-Effectors for Grasping Space Debris”. In: *2023 Regional Student Conferences*. DOI: [10.2514/6.2023-71045](https://doi.org/10.2514/6.2023-71045). eprint: <https://arc.aiaa.org/doi/pdf/10.2514/6.2023-71045>. URL: <https://arc.aiaa.org/doi/abs/10.2514/6.2023-71045> (cit. on p. 28).

- [14] ESA. *Space Environment Statistics*. 2025. URL: <https://sdup.esoc.esa.int/discosweb/statistics/> (visited on 05/25/2025) (cit. on p. 37).
- [15] Minghe Shan, Jian Guo, and Eberhard Gill. “Review and comparison of active space debris capturing and removal methods”. In: *Progress in Aerospace Sciences* 80 (2016), pp. 18–32. ISSN: 0376-0421. DOI: <https://doi.org/10.1016/j.paerosci.2015.11.001>. URL: <https://www.sciencedirect.com/science/article/pii/S0376042115300221> (cit. on pp. 37, 38).
- [16] C. Priyant Mark and Surekha Kamath. “Review of Active Space Debris Removal Methods”. In: *Space Policy* 47 (2019), pp. 194–206. ISSN: 0265-9646. DOI: <https://doi.org/10.1016/j.spacepol.2018.12.005>. URL: <https://www.sciencedirect.com/science/article/pii/S0265964618300110> (cit. on pp. 37, 38).
- [17] Alexander Ledkov and Vladimir Aslanov. “Review of contact and contactless active space debris removal approaches”. In: *Progress in Aerospace Sciences* 134 (2022), p. 100858. ISSN: 0376-0421. DOI: <https://doi.org/10.1016/j.paerosci.2022.100858>. URL: <https://www.sciencedirect.com/science/article/pii/S0376042122000501> (cit. on pp. 37–40).
- [18] Robin Biesbroek, Sarmad Aziz, Andrew Wolahan, Ste-fano Cipolla, Muriel Richard-Noca, and Luc Piguet. “The clearspace-1 mission: ESA and clearspace team up to remove debris”. In: *Proc. 8th Eur. Conf. Sp. Debris*. 2021, pp. 1–3 (cit. on p. 38).
- [19] Y. Tsuda, O. Mori, R. Funase, H. Sawada, T. Yamamoto, T. Saiki, T. Endo, and J. Kawaguchi. “Flight status of IKAROS deep space solar sail demonstrator”. In: *Acta Astronautica* 69.9 (2011), pp. 833–840. ISSN: 0094-5765. DOI: <https://doi.org/10.1016/j.actaastro.2011.06.005>. URL: <https://www.sciencedirect.com/science/article/pii/S0094576511001822> (cit. on p. 38).
- [20] David A. Spencer, Bruce Betts, John M. Bellardo, Alex Diaz, Barbara Plante, and Justin R. Mansell. “The LightSail 2 solar sailing technology demonstration”. In: *Advances in Space Research* 67.9 (2021). Solar Sailing: Concepts, Technology, and Missions II, pp. 2878–2889. ISSN: 0273-1177. DOI: <https://doi.org/10.1016/j.asr.2020.06.029>. URL: <https://www.sciencedirect.com/science/article/pii/S027311772030449X> (cit. on p. 38).
- [21] Yasushi Ohkawa, Satomi Kawamoto, Teppei Okumura, Kentaro Iki, Hiroyuki Okamoto, Koichi Inoue, Takashi Uchiyama, and Daisuke Tsujita. “Review of KITE - Electrodynamic tether experiment on the H-II Transfer Vehicle”. In: *Acta Astronautica* 177 (2020), pp. 750–758. ISSN: 0094-5765. DOI: <https://doi.org/10.1016/j.actaastro.2020.03.014>. URL: <https://www.sciencedirect.com/science/article/pii/S0094576520301429> (cit. on p. 39).
- [22] G. Sánchez-Arriaga et al. “The E.T.PACK project: Towards a fully passive and consumable-less de-orbit kit based on low-work-function tether technology”. In: *Acta Astronautica* 177 (2020), pp. 821–827. ISSN: 0094-5765. DOI: <https://doi.org/10.1016/j.actaastro.2020.03.036>. URL: <https://www.sciencedirect.com/science/article/pii/S0094576520301648> (cit. on p. 39).
- [23] L. Tarabini Castellani et al. “Deorbit kit demonstration mission”. In: *Journal of Space Safety Engineering* 9.2 (2022), pp. 165–173. ISSN: 2468-8967. DOI: <https://doi.org/10.1016/j.jsse.2022.01.004>. URL: <https://www.sciencedirect.com/science/article/pii/S2468896722000040> (cit. on p. 39).
- [24] Gonzalo Sánchez-Arriaga, Enrico C. Lorenzini, and Sven G. Bilén. “A review of electrodynamic tether missions: Historical trend, dimensionless parameters, and opportunities opening space markets”. In: *Acta Astronautica* 225 (2024), pp. 158–168. ISSN: 0094-5765. DOI: <https://doi.org/10.1016/j.actaastro.2024.09.002>. URL: <https://www.sciencedirect.com/science/article/pii/S0094576524004971> (cit. on p. 40).
- [25] Joseph Carroll and John Oldson. “Tethers for small satellite applications”. In: (1995) (cit. on p. 40).

- [26] C Le. *Tepce: A tethered electrodynamic propulsion cubesat experiment*. 2022 (cit. on p. 40).
- [27] Robert Forward and Robert Hoyt. “Failsafe multiline Hoytether lifetimes”. In: *31st Joint Propulsion Conference and Exhibit*. DOI: [10.2514/6.1995-2890](https://doi.org/10.2514/6.1995-2890). URL: <https://arc.aiaa.org/doi/abs/10.2514/6.1995-2890> (cit. on p. 41).
- [28] Petri Toivanen, Pekka Janhunen, Jarmo Kivekäs, and Meri Mäkelä. “Robust Flight Tether for In-Orbit Demonstrations of Coulomb Drag Propulsion”. In: *Aerospace* 11.1 (2024). ISSN: 2226-4310. DOI: [10.3390/aerospace11010062](https://doi.org/10.3390/aerospace11010062). URL: <https://www.mdpi.com/2226-4310/11/1/62> (cit. on p. 41).
- [29] Harrison C Stankey and Robert P Hoyt. “In-Flight Performance of the Terminator Tape End-of-Life Deorbit Module”. In: (2021) (cit. on p. 41).
- [30] P. Kelly, E. Glad, and T. Ritz. “A Summary of the DRAGRACER Flight Experiment for Orbital Debris Mitigation and Radiometric Solutions”. In: *Proceedings of the Advanced Maui Optical and Space Surveillance (AMOS) Technologies Conference*. Ed. by S. Ryan. Sept. 2023, 6, p. 6 (cit. on p. 41).